Gastroenterology 2019;157:210–226

Ccne1 Overexpression Causes Chromosome Instability in Liver Cells and Liver Tumor Development in Mice

Khaled Aziz,[1,*] **Jazeel F. Limzerwala**,[1,*] **Ines Sturmlechner**,[2,3,*] **Erin Hurley**,[2,*] Cheng Zhang,[4] Karthik B. Jeganathan,[2] Grace Nelson,[2] Steve Bronk,[5] Raul O. Fierro Velasco,[2] Erik-Jan van Deursen,[2] Daniel R. O'Brien,[6,7] Jean-Pierre A. Kocher,[6,7] Sameh A. Youssef,[8] Janine H. van Ree,[2] Alain de Bruin,[3,8] Hilda van den Bos,[9] Diana C. J. Spierings,[9] Floris Foijer,[9] Bart van de Sluis,[3] Lewis R. Roberts,[5] Gregory J. Gores,[5] Hu Li,[4] and Jan M. van Deursen[1,2,3]

[1]Department of Biochemistry and Molecular Biology, Mayo Clinic, Rochester, Minnesota; [2]Department of Pediatric and Adolescent Medicine, Mayo Clinic, Rochester, Minnesota; [3]Department of Pediatrics, University of Groningen, University Medical Center Groningen, Groningen, The Netherlands; [4]Department of Molecular Pharmacology and Experimental Therapeutics, Mayo Clinic, Rochester, Minnesota; [5]Department of Gastroenterology and Hepatology, Mayo Clinic, Rochester, Minnesota; [6]Department of Biomedical Statistics and Informatics, Mayo Clinic, Rochester, Minnesota; [7]Department of Health Sciences Research, Mayo Clinic, Rochester, Minnesota; [8]Department of Pathobiology, Faculty of Veterinary Medicine, Utrecht University, Utrecht, The Netherlands; and [9]European Research Institute for the Biology of Ageing (ERIBA), University of Groningen, University Medical Center Groningen, Groningen, The Netherlands

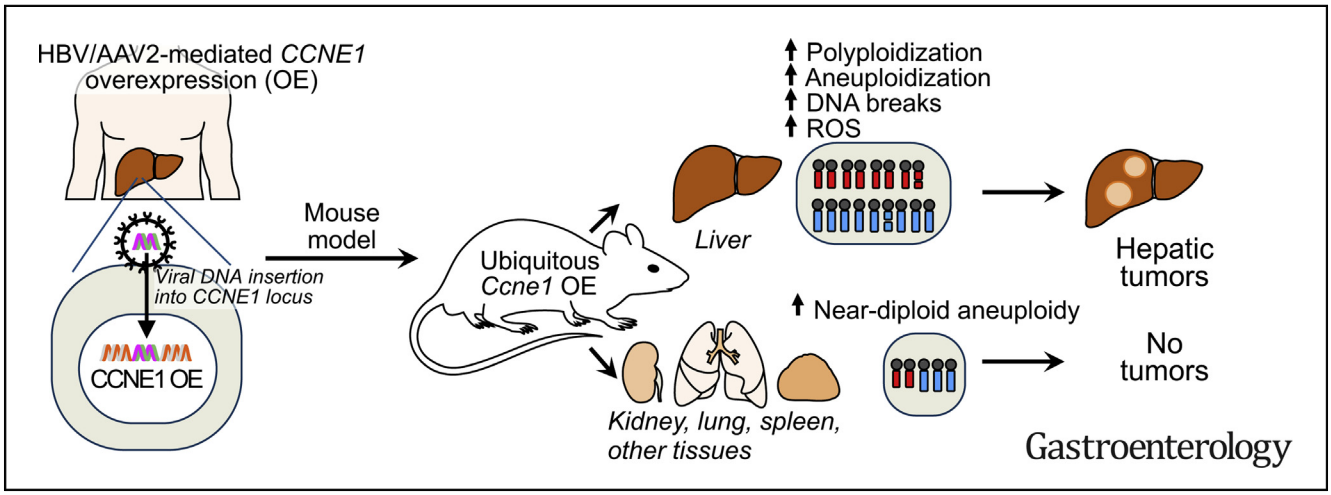

See Covering the Cover Synopsis on 2.

BACKGROUND & AIMS: The *CCNE1* locus, which encodes cyclin E1, is amplified in many types of cancer cells and is activated in hepatocellular carcinomas (HCCs) from patients infected with hepatitis B virus or adeno-associated virus type 2, due to integration of the virus nearby. We investigated cell-cycle and oncogenic effects of cyclin E1 overexpression in tissues of mice. **METHODS:** We generated mice with doxycycline-inducible expression of *Ccne1* (*Ccne1*^{T} mice) and activated overexpression of cyclin E1 from age 3 weeks onward. At 14 months of age, livers were collected from mice that overexpress cyclin E1 and nontransgenic mice (controls) and analyzed for tumor burden and by histology. Mouse embryonic fibroblasts (MEFs) and hepatocytes from *Ccne1*^{T} and control mice were analyzed to determine the extent to which cyclin E1 overexpression perturbs S-phase entry, DNA replication, and numbers and structures of chromosomes. Tissues from 4-month-old *Ccne1*^{T} and control mice (at that age were free of tumors) were analyzed for chromosome alterations, to investigate the mechanisms by which cyclin E1 predisposes hepatocytes to transformation. **RESULTS:** *Ccne1*^{T} mice developed more hepatocellular adenomas and HCCs than control mice. Tumors developed only in livers of *Ccne1*^{T} mice, despite high levels of cyclin E1 in other tissues. *Ccne1*^{T} MEFs had defects that promoted chromosome missegregation and aneuploidy, including incomplete replication of DNA, centrosome amplification, and formation of nonperpendicular mitotic spindles. Whereas *Ccne1*^{T} mice accumulated near-diploid aneuploid cells in multiple tissues and organs, polyploidization was observed only in hepatocytes, with losses and gains of whole chromosomes, DNA damage, and oxidative stress. **CONCLUSIONS:** Livers, but not other tissues of mice with inducible overexpression of cyclin E1, develop tumors. More hepatocytes from the cyclin E1–overexpressing mice were polyploid than from control mice, and had losses or gains of whole chromosomes, DNA damage, and oxidative stress; all of these have been observed in human HCC cells. The increased risk of HCC in patients with hepatitis B virus or

adeno-associated virus type 2 infection might involve activation of cyclin E1 and its effects on chromosomes and genomes of liver cells.

Keywords: AAV2; HBV; Chromosome Integrity; Hepatocarcinogenesis.

WHAT YOU NEED TO KNOW

BACKGROUND

The *CCNE1* locus, which encodes cyclin E1, is amplified in many types of cancer cells and is activated in hepatocellular carcinomas (HCCs) from patients infected with hepatitis B virus or adeno-associated virus type 2, due to integration of the virus nearby. We investigated cell cycle-related defects that result from cyclin E1 overexpression in mice.

FINDINGS

Livers, but not other tissues of mice with inducible overexpression of cyclin E1, develop tumors. Hepatocytes from these mice have increased polyploidization, losses and gains of whole chromosomes, DNA damage, and oxidative stress —all of these have been observed in human HCC cells.

LIMITATIONS

This study was performed in mice.

IMPLICATIONS FOR PATIENT CARE

The increased risk of HCC in patients with hepatitis B virus or adeno-associated virus type 2 infection might involve activation of cyclin E1 and its effects on chromosomes and genomes of liver cells.

Complexes of CDK2 and E-type cyclins (E1 and E2) trigger S-phase entry through phosphorylation of specific substrates, including members of the retinoblastoma protein (RB) family.[1,2] Combined genetic inactivation of cyclin E1 and E2 results in embryonic lethality during mid-gestation with placental and cardiac defects.[3,4] Elegant follow-up experiments using conditional knockout alleles in which ablation of E-type cyclins was postponed until the end of embryogenesis revealed that cyclin E1 and E2 are dispensable for postnatal growth and viability.[5] Interestingly, however, when E-type cyclin-deficient mice were challenged with a carcinogen that causes liver cancer, they were found to be protected against tumor formation, indicating that, in contrast to normal cells, neoplastic cells cannot progress through S-phase in the absence of E-type cyclins. This dependence of tumor cells has been linked to CDK-independent functions of E-type cyclins in loading MCM helicase onto chromatin-bound CDT1.[5,6] Collectively, these insights led to speculation that agents targeting E-type cyclins could provide successful protection against tumor cell proliferation while leaving normal cells unperturbed.[5]

In addition to being required for tumor cell proliferation, cyclin E1 has been widely documented to be overexpressed in multiple human cancers, including ovarian, breast, lung, and liver cancers, where it is thought to result in premature S-phase entry, ineffective DNA replication, and genomic instability.[7–9] Cell-cycle regulators are often expressed at elevated levels in human malignancies, which arguably could be a consequence of an increased mitotic index. However, this is unlikely to apply to cyclin E1 because the *CCNE1* gene locus is frequently amplified in human tumors.[10] Furthermore, recent studies have identified the *CCNE1* locus as a viral integration site in 2% to 5% of hepatocellular carcinomas (HCCs) of patients infected with hepatitis B virus (HBV), resulting in marked up-regulation of *CCNE1* expression in tumorous vs normal liver tissue, presumably by viral enhancer elements.[11–14] More than 50% of patients with HCC worldwide are expected to develop from the estimated 350 million chronic HBV carriers,[15] who have a 100-fold increased risk for acquiring HCC. A substantial number of patients with HCC are therefore expected to have an HBV integration in *CCNE1*. The respiratory virus AAV2 (adeno-associated virus) infects up to 50% of the population.[16] It is largely considered nonpathogenic and AAV2 derivatives are used in gene therapy approaches. However, recent studies have documented clonal insertions of AAV2 in 6% of HCC cases,[17] sparking debate about the safety of these viral vectors in clinical trials. Importantly, one study reported that 3 of 11 HCC tumors with clonal AAV2 insertions showed viral integration in the *CCNE1* locus.[17]

Here we investigated the consequences of cyclin E1 overexpression in mice using a doxycycline (dox)-inducible ubiquitous promoter. We found that these mice are prone to hepatocellular adenomas and HCCs and that hepatocytes with high levels of cyclin E1 have multiple features of human HCC cells, including increased polyploidization, losses and gains of whole chromosomes, DNA damage, and oxidative stress.

Methods

Mouse Strains

All mice were housed in a pathogen-free barrier environment. Mouse protocols were reviewed and approved by the Mayo Clinic Institutional Animal Care and Use Committee. All animals were maintained on a mixed 129/Sv × C57BL/6 genetic background. *Ccne1-HA* (polymerase chain reaction–amplified *Ccne1* cDNA with 3′ hemagglutinin [HA] tag) transgenic mice were generated using KH2 embryonic stem (ES) cells (Origene Technologies, Rockville, MD) according to previously described

***Authors share co-first authorship.**

Abbreviations used in this paper: **AAV2, adeno-associated virus; CIN, chromosomal instability; dox, doxycycline; DSB, double-stranded DNA break; ES, embryonic stem; FACS, fluorescence-activated cell sorter; FISH, fluorescence in situ hybridization; HA, hemagglutinin; HBV, hepatitis B virus; HCC, hepatocellular carcinoma; MEF, mouse embryonic fibroblast; RB, retinoblastoma protein.**

Most current article

0016-5085/$36.00
https://doi.org/10.1053/j.gastro.2019.03.016

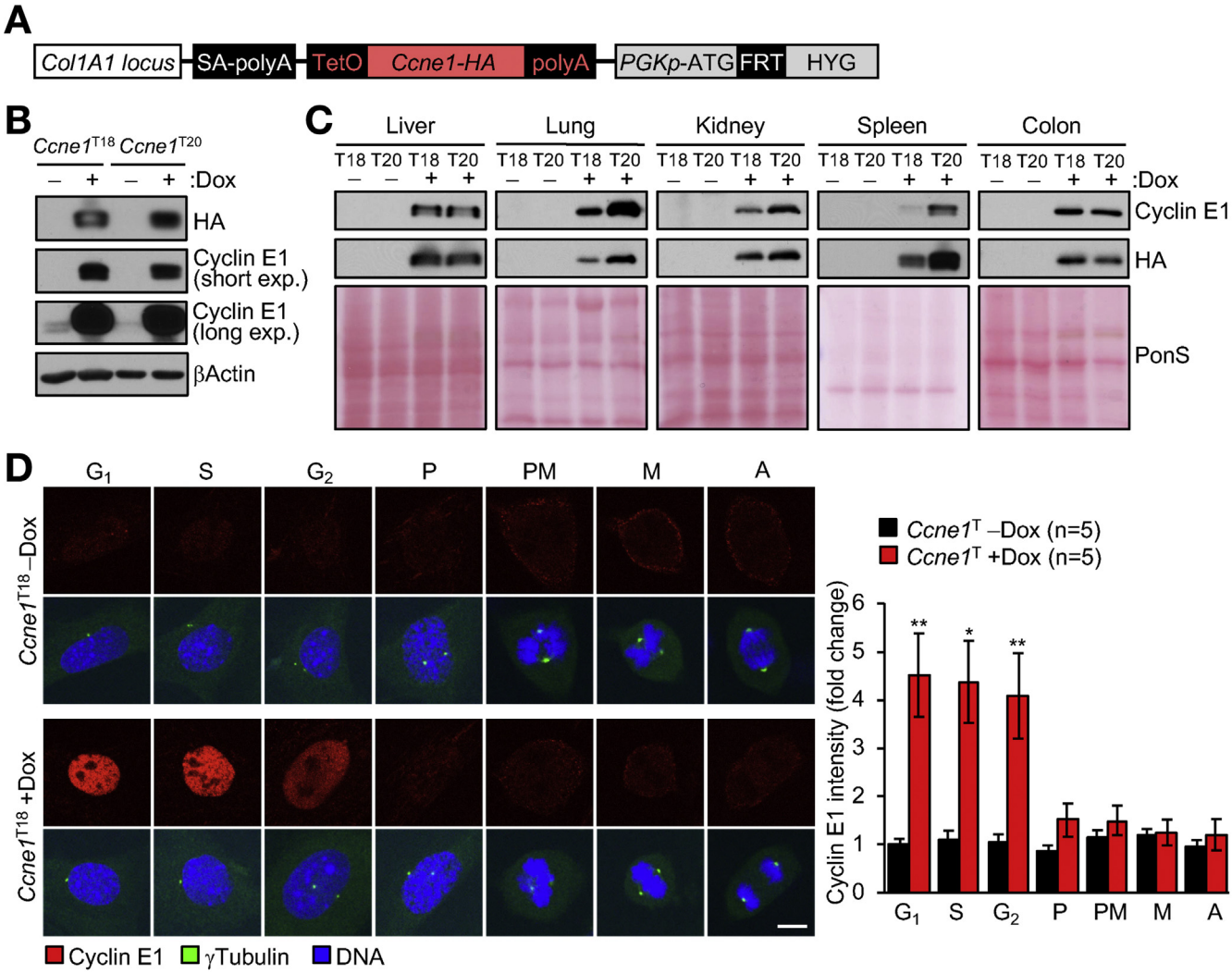

Figure 1. Generation of *Ccne1* transgenic mice. (*A*) *Ccne1* transgene integrated in the *Col1A1* locus. (*B*) Western blots of lysates of *Ccne1*^{T} MEFs cultured in the presence or absence of dox for 72 hours and probed for HA and cyclin E1. β-actin served as loading control. (*C*) Western blots of tissue extract from the indicated 6-week-old transgenic mice. Ponceau S (PonS) staining of blotted proteins served as a loading control. (*D*) *Left*: MEFs at various stages of cell cycle stained for cyclin E1. γTubulin staining was used for cell-cycle staging. P, Prophase; PM, Prometaphase; M, Metaphase; A, Anaphase. *Right*: Quantification of cyclin E1 signals (normalized to -dox G_1 expression). Data represent mean ± SEM. Statistics: (*D*) 2-tailed paired *t* test. *$P < .05$, **$P < .01$. Scale bar, 5 μm.

methods.[18] KH2 ES clones properly expressing *Ccne1-HA* were injected into blastocysts, and chimeras from 2 independent *Ccne1-HA* (*Ccne1*^{T18} and *Ccne1*^{T20}) clones achieved germline transmission. These transgenes were maintained on M2-rtTA (TA) hemizygous background (*ROSA26*). Both sexes were used for experimentation. At 3 weeks of age, transgenic mice were continuously administered 2 mg/mL dox (#690902; Letco Medical, Decatur, AL) in drinking water containing 5% sucrose. At 14 months, mice were humanely killed and major organs were screened for overt tumors. Separate cohorts of mice were generated where dox was administered between 3 and 5, 5 and 7, or 3 and 16 weeks of age.

Generation and Culture of Mouse Embryonic Fibroblasts

Ccne1^{T18} and *Ccne1*^{T20} mouse embryonic fibroblasts (MEFs) were generated at embryonic day 13.5 and cultured as previously described.[19] At least 3 independently generated MEF lines per genotype were used. Mitotic MEFs were prepared by culturing asynchronous cells for 5 hours in medium containing 100 ng/mL nocodazole (#M1404; Sigma-Aldrich, St Louis, MO) and harvesting cells by "shake-off." Monastrol washout was carried out by sequentially treating MEFs with monastrol (#BML-GR322; Enzo Life Sciences, Farmingdale, NY) for 1 hour, monastrol and MG132 (#C2211; Sigma-Aldrich) for 1 hour followed by MG132 alone for 90 minutes. Cells were then fixed with phosphate-buffered saline/4% paraformaldehyde for 10 minutes and stained with Hoechst.

Hepatocyte Isolation and Ploidy Analysis

Hepatocytes from mouse livers were isolated by collagenase perfusion through the hepatic portal vein as described previously.[20] Hepatocytes were purified by Percoll gradient centrifugation, counted, and 1 million cells were used for propidium

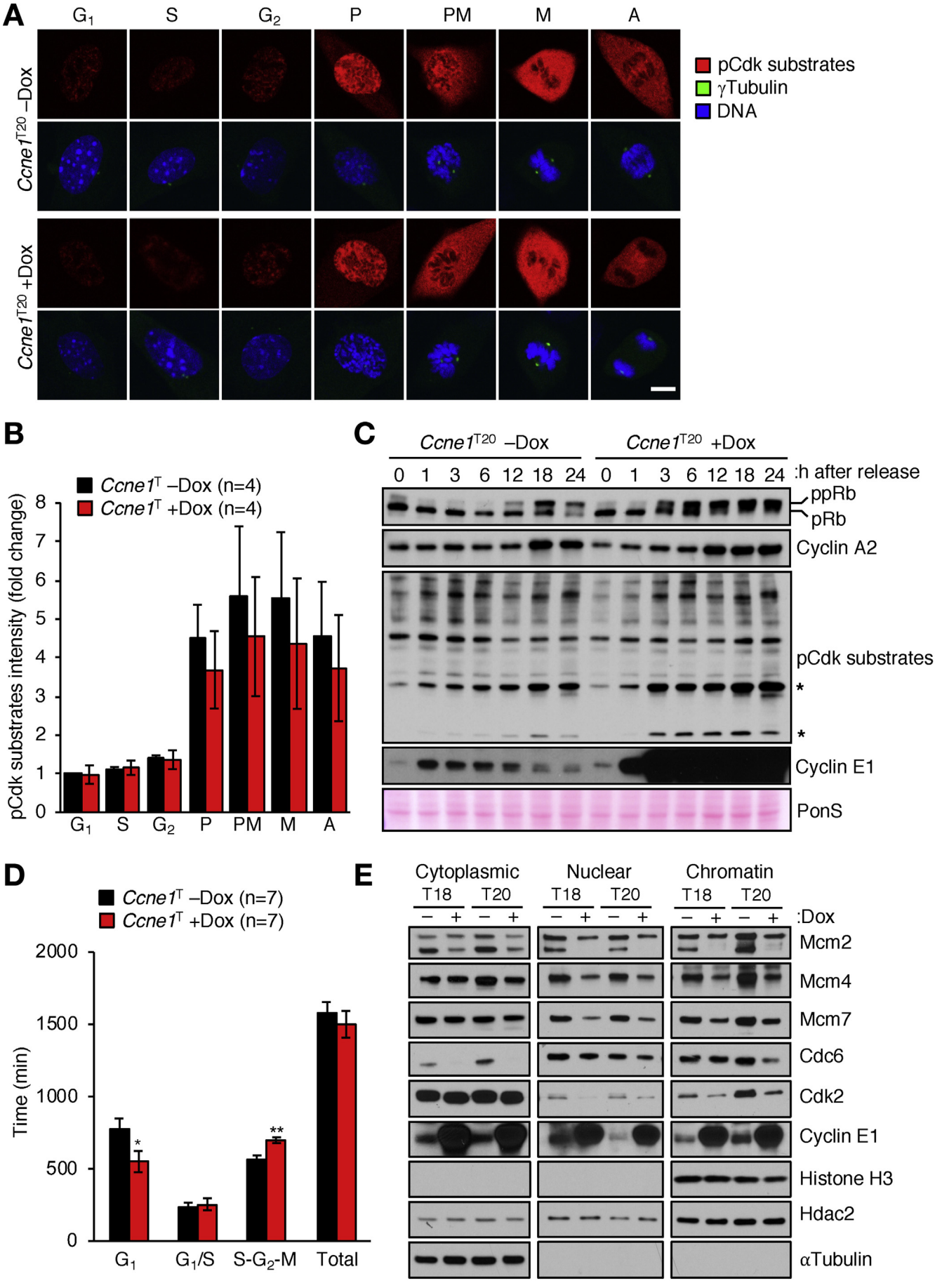
A
G1
S
G2
P
PM
M
A
Ccne1T20 –Dox
Ccne1T20 +Dox
pCdk substrates
γTubulin
DNA
B
Ccne1T –Dox (n=4)
Ccne1T +Dox (n=4)
pCdk substrates intensity (fold change)
C
Ccne1T20 –Dox
Ccne1T20 +Dox
:h after release
ppRb
pRb
Cyclin A2
pCdk substrates
Cyclin E1
PonS
D
Ccne1T –Dox (n=7)
Ccne1T +Dox (n=7)
Time (min)
G1
G1/S
S-G2-M
Total
E
Cytoplasmic
Nuclear
Chromatin
T18
T20
:Dox
Mcm2
Mcm4
Mcm7
Cdc6
Cdk2
Cyclin E1
Histone H3
Hdac2
αTubulin

iodide staining and fluorescence-activated cell sorting (FACS) analysis. Flow data were analyzed via pulse shape analysis in FlowJo 6.4.7 (FlowJo, Ashland, OR).

Partial Hepatectomy

Partial hepatectomies were performed on 8- to 10-week-old male mice, induced with dox from 3 weeks of age, as described.[21] Forty-eight hours after the surgery, mice were killed, and the liver lobes were collected and fixed in phosphate-buffered saline/4% paraformaldehyde for immunostaining.

Western Blot Analysis

Western blot analysis was carried out as previously described.[19] Subcellular fractionation was performed per manufacturer's protocol (#78840 or #87790; Thermo Scientific, Waltham, MA). Primary antibodies used for Western blotting are listed in Supplementary Table 1.

Statistical Analyses

GraphPad Prism software (LaJolla, CA) was used for all statistical analyses. Graphs are indicated with the significance score of $*P < .05$, $**P < .01$, and $***P < .001$. We note that no power calculations were used. Sample sizes were based on previously published experiments where differences were observed. No samples were excluded. Investigators were not blinded to allocation during experiments and outcome assessment.

Aneuploidy Analyses

Chromosome counts were carried out on metaphase spreads from Colcemid-treated transgenic MEFs grown in the presence or absence of dox for 48 hours or on splenocytes of 5-month-old transgenic mice treated with dox since weaning.[19] Interphase fluorescence in situ hybridization (FISH) analysis with probes for chromosomes 4 and 7 was carried out on single-cell suspensions of various tissues and tumors as previously described.[19]

Single-Cell Whole Genome Sequencing

Single-cell whole genome sequencing on liver tissue from 4-month-old mice (on dox from weaning) was performed as described previously.[22] FACS-sorted tetraploid (4n) cells were exclusively used for preparing libraries and sequencing. Copy number alterations and segmental aneuploidy score were determined using the AneuFinder software.[22]

In Vitro Kinase Assay

Kinase assays were performed as previously described.[23]

Additional methods are described in the Supplementary Section.

Results

Generation of Cyclin E1–Overexpressing Mice

To achieve ubiquitous overexpression of full-length cyclin E1 in mice, we generated dox-inducible *Ccne1* transgenic animals using FLP/Frt-mediated site-directed integration 3′ of the *Col1A1* locus of KH2 ES cells (Figure 1*A*).[18] Two independent transgenic strains were obtained, referred to as $Ccne1^{T18}$ and $Ccne1^{T20}$ (in experiments in which both lines were used interchangeably, they are denoted as $Ccne1^{T}$). Tissues and MEFs from both strains showed high overexpression of cyclin E1 protein in the presence of dox, whereas no transgene expression was observed in its absence (Figure 1*B* and C, Supplementary Figure 1*A*). In MEFs, both protein and transcript levels were elevated approximately 40-fold (Supplementary Figure 1*B* and *C*).

Cyclin E1 Overexpression Disrupts Cdk-dependent and -independent Functions

Cyclin E1 levels of dox-treated MEFs were highly elevated in G_1, S, and G_2 phase, yet normal in mitosis, suggesting that proteolytic degradation occurs before M phase entry (Figure 1*D*). Immunolabeling of MEFs with an antibody against phosphorylated Cdk substrates suggested that cyclin E1 overexpression had no impact on global Cdk activity (Figure 2*A* and *B*). Furthermore, Cdk2 immunoprecipitated from asynchronous $Ccne1^{T}$ MEFs cultured in the presence of dox did not show elevated activity in an in vitro kinase assay with Histone H1 as substrate (Supplementary Figure 2). On the other hand, serum-starved $Ccne1^{T}$ MEFs released in serum-containing medium with dox showed accelerated phosphorylation of Rb1 and precocious S-phase entry as evidenced by the premature induction of cyclin A2 (Figure 2*C*). Consistent with this, fluorescence ubiquitination cell-cycle indicator (FUCCI) analysis revealed a significant shortening of G_1 phase in dox-treated $Ccne1^{T}$ MEFs (Figure 2*D*). Furthermore, a small subset of proteins detected by the pan Cdk substrate antibody on immunoblots was expressed at elevated levels in these cells (Figure 2*C*), implying that cyclin E1 overexpression alters Cdk substrate phosphorylation in a select rather than a global manner.

Cyclin E1 also has a Cdk-independent function in loading the MCM DNA helicase complex onto origins of replication to drive initiation and elongation of DNA replication in S-phase.[5,6] To examine whether this function was perturbed with cyclin E1 overexpression, we compared cytoplasmic, nuclear, and chromatin-associated levels of key MCM proteins between dox-treated and untreated $Ccne1^{T}$ MEFs, including Mcm2, 4, and 7. All 3 of these proteins were

Figure 2. High transgenic expression of cyclin E1 alters cell-cycle timing. (*A*) Representative images of dox-treated and untreated $Ccne1^{T}$ MEFs at the indicated stages of cell cycle immunolabeled for phosphorylated Cdk substrates. Scale bar, 5 μm. (*B*) Quantification of phosphorylated Cdk (pCdk) substrate signals of the indicated MEFs at various stages of the cell cycle (normalized to -dox G_1 signals). (*C*) Western blots of lysates of $Ccne1^{T}$ MEFs harvested at the indicated time points after release from serum starvation in the presence or absence of dox. *Asterisks* mark hyperphosphorylated Cdk substrates. (*D*) Analysis of the indicated MEFs by fluorescence ubiquitination cell-cycle indicator technology. (*E*) Western blots of fractionated lysates of MEFs grown with or without dox for 72 hours. Histone H3, Hdac2, and αTubulin represent chromatin, nuclear, and cytoplasmic markers, respectively. Data in (*B*) and (*D*) represent mean ± SEM. Statistics: (*B*) and (*D*), 2-tailed paired *t* test. $*P < .05$, $**P < .01$.

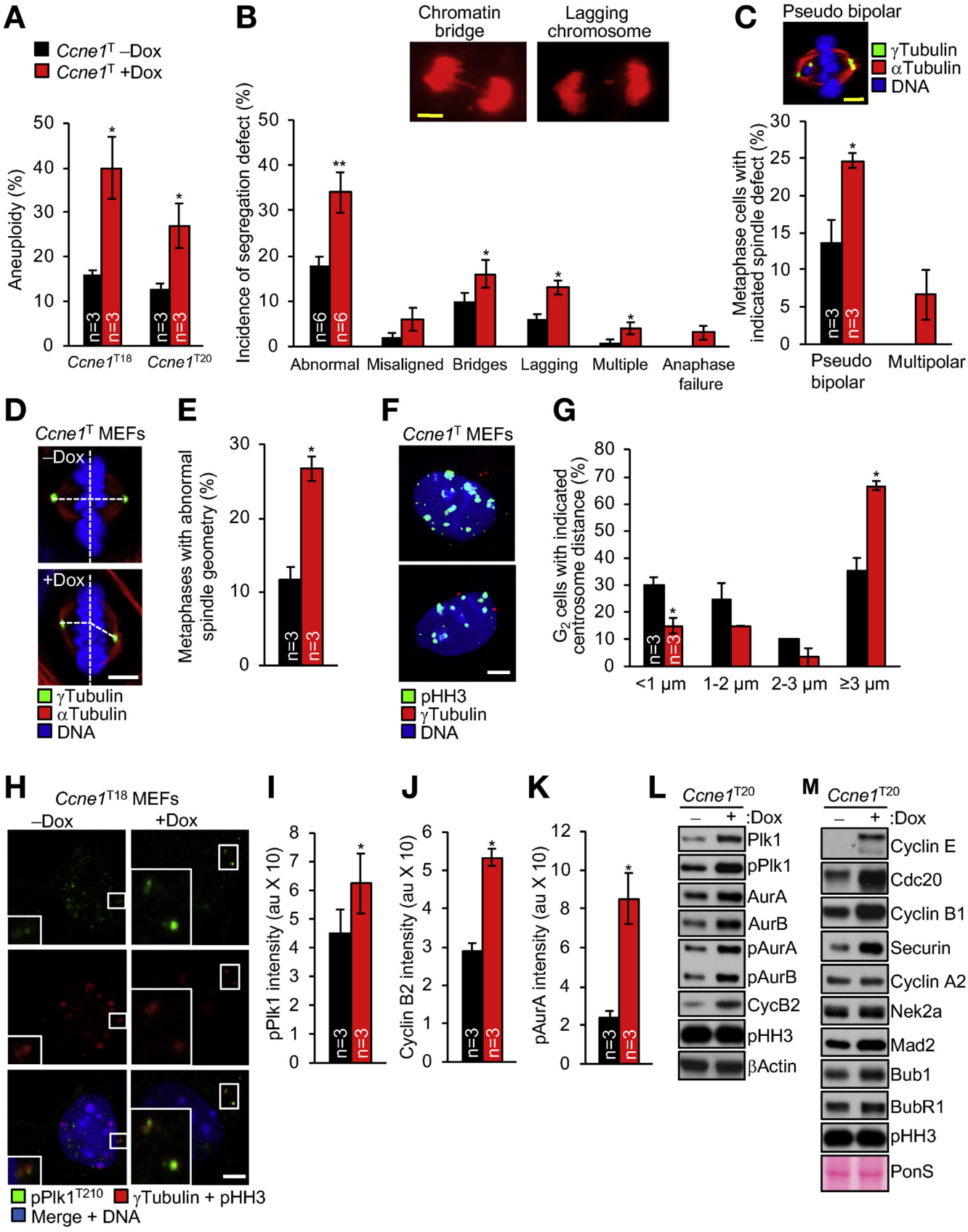
A
Ccne1T –Dox
Ccne1T +Dox
Aneuploidy (%)
Ccne1T18
Ccne1T20
B
Chromatin bridge
Lagging chromosome
Incidence of segregation defect (%)
Abnormal
Misaligned
Bridges
Lagging
Multiple
Anaphase failure
C
Pseudo bipolar
γTubulin
αTubulin
DNA
Metaphase cells with indicated spindle defect (%)
Pseudo bipolar
Multipolar
D
Ccne1T MEFs
–Dox
+Dox
γTubulin
αTubulin
DNA
E
Metaphases with abnormal spindle geometry (%)
F
Ccne1T MEFs
pHH3
γTubulin
DNA
G
G2 cells with indicated centrosome distance (%)
<1 μm
1-2 μm
2-3 μm
≥3 μm
H
Ccne1T18 MEFs
–Dox
+Dox
pPlk1T210
γTubulin + pHH3
Merge + DNA
I
pPlk1 intensity (au X 10)
J
Cyclin B2 intensity (au X 10)
K
pAurA intensity (au X 10)
L
Ccne1T20
:Dox
Plk1
pPlk1
AurA
AurB
pAurA
pAurB
CycB2
pHH3
βActin
M
Ccne1T20
:Dox
Cyclin E
Cdc20
Cyclin B1
Securin
Cyclin A2
Nek2a
Mad2
Bub1
BubR1
pHH3
PonS

reduced in both the nuclear and chromatin fractions of cyclin E1 overexpressing cells (Figure 2*E*), predicting DNA replication stress and chromosomal instability (CIN). Furthermore, cytoplasmic levels of Mcm2, but not Mcm4 and 7, were also reduced.

Cyclin E1 Overexpression Causes a Complex CIN Phenotype in MEFs

To examine the impact of cyclin E1 overexpression on CIN, we prepared metaphase spreads of *Ccne1*^{T} MEFs cultured in the presence or absence of dox and performed chromosome counts. Aneuploidy rates were indeed elevated with cyclin E1 overexpression (Figure 3*A* and Supplementary Figure 3*A*). Consistent with this, live-cell imaging of *Ccne1*^{T} MEFs stably overexpressing H2B-mRFP demonstrated that chromosome missegregation rates were elevated in the presence of dox, with both lagging chromosomes and chromatin bridges driving the increase (Figure 3*B*). Phosphorylation of Chk1 at Ser345, a marker of replication stress associated with chromatin bridge formation,[24] was elevated in dox-treated *Ccne1*^{T} MEFs (Supplementary Figure 3*B*). Fluorescence ubiquitination cell-cycle indicator analysis (FUCCI) revealed that cyclin E1 overexpression extends S-G_2-M, providing further evidence for replication stress (Figure 2*D*). Furthermore, DNA fiber assays showed that cyclin E1 overexpression increases replication fork stalling (Supplementary Figure 3*C*). Unreplicated single-stranded DNA at stalled replication forks is vulnerable to breakage. Indeed, in immunolabeling experiments for γH2AX, 53BP1, and RPA2, cyclin E1 overexpressing MEFs showed elevated rates of double-stranded DNA breaks (DSBs; Supplementary Figure 3*D* and *E*). Furthermore, cyclin E1 overexpressing cells had high p53 activity, a feature of cells with DSBs (Supplementary Figure 3*F*). These data indicate that incomplete DNA replication contributes to chromatin bridge formation in cyclin E1–overexpressing MEFs.

Next, we assessed how cyclin E1 overexpression promotes the formation of merotelic attachments that produce lagging chromosomes. These attachments can form through multiple mechanisms, including centrosome amplification,[25] aberrant centrosome disjunction or movement,[26] defective attachment error correction,[27] and accelerated mitotic timing. Error correction and timing of mitoses were not affected by cyclin E1 overexpression (Supplementary Figure 3*G* and *H*); however, cyclin E1 overexpression led to the formation of merotely prone pseudobipolar mitotic spindles with supernumerary centrosomes, as revealed by immunolabeling for γTubulin and αTubulin (Figure 3*C*). Furthermore, spindle poles of cyclin E1 overexpressing MEFs with normal centrosome numbers frequently failed to align perpendicularly to the metaphase plate (Figure 3*D* and *E*). Such nonperpendicular spindles can result from aberrant disjunction or movement of duplicated centrosomes, and are a source of merotelic attachments.[26] Analysis of γTubulin-stained MEFs revealed that centrosome disjunction in G_2 was accelerated at high cyclin E1 levels (Figure 3*F* and *G*), a phenotype that is consistent with the aberrantly high levels of centrosome-associated cyclin B2, pAurA, and pPlk1 (Figure 3*H–K* and Supplementary Figure 4*A* and *B*).[19] Western blot analysis of lysates of prometaphase-arrested MEFs confirmed that cyclin B2, Plk1, pPlk1, AurA, and pAurA levels were elevated with cyclin E1 overexpression, as were AurB and pAurB (Figure 3*L*). All these mitotic regulators are E2F target genes, further supporting that cyclin E1 overexpression deregulates Cdk activity. We note that even though centrosome-association and phosphorylation of Eg5 were unperturbed (Supplementary Figure 4*C* and *D*), a small proportion of cyclin E1 transgenic MEFs showed slow centrosome movement, which could contribute to lagging chromosome formation (Supplementary Figure 4*E*).

The observation that cyclin E1 overabundance increases the expression of key regulators of bipolar spindle assembly prompted us to conduct a more comprehensive analysis of mitotic regulator levels in mitotic shake-off lysates of dox-treated and untreated MEFs (Figure 3*M*). Cdc20, a key activator of APC/C, was highly elevated in dox-treated *Ccne*^{T20} MEFs. Key substrates of APC/C^{Cdc20} were either present at normal levels, such as Nek2a and cyclin A2, or substantially elevated, such as securin and cyclin B1. Securin and cyclin B1 both inhibit separase-mediated cleavage of cohesin, raising the possibility that their overabundance causes anaphase bridge formation through nondisjunction of sister chromosomes. Even though 2 core mitotic checkpoint proteins, Bub1 and Mad2, were mildly elevated, spindle assembly checkpoint activity remained unperturbed with cyclin E1 overexpression (Supplementary Figure 4*F*). The observed increases in cyclin B1, Mad2, Bub1, and securin may be because they are transcriptionally regulated by E2F.[28] Nek2a and cyclin A2 are as well, but they are not elevated, which could be because of increased APC/C^{Cdc20}-driven proteasomal degradation. Collectively,

Figure 3. Cyclin E1 overexpression causes chromosome segregation errors and aneuploidy in MEFs. (*A*) Chromosome counts on metaphase spreads of the indicated MEFs. (*B*) Chromosome segregation analysis of MEFs expressing H2B-mRFP. Images: *Ccne1*^{T} MEFs with indicated segregation errors. (*C*) Incidence of pseudobipolar or multipolar spindles in metaphases stained for αTubulin and γTubulin. Image: *Ccne1*^{T} MEF with indicated spindle defect. (*D*) Representative metaphases with perpendicular (*top*) and nonperpendicular spindles (*bottom*). (*E*) Incidence of nonperpendicular metaphase spindles. (*F*) Representative images of G_2 MEFs with normal (*top*) and premature (*bottom*) centrosome disjunction. (*G*) Measurements of centrosome separation in G_2 MEFs staged for equal phospho-histone H3^{Ser10} (pHH3) expression. (*H*) Representative images of pPlk1-stained prophases grown with and without dox. (*I*) Quantification of pPlk1 levels at centrosomes (normalized to γTubulin levels). (*J*, *K*) As in (*H*) for cyclin B2 and pAurA, respectively. (*L*, *M*) Western blots of mitotic shake-off lysates probed for the indicated proteins. Data in (*A–C*), (*E*), (*G*), (*I–K*) represent mean ± SEM. Statistics: (*A*, *B*, *E*, *G*, *I–K*) 2-tailed paired *t* test; (*C*) 2-tailed unpaired *t* test. $^{*}P < .05$, $^{**}P < .01$. Scale bars, 5 μm.

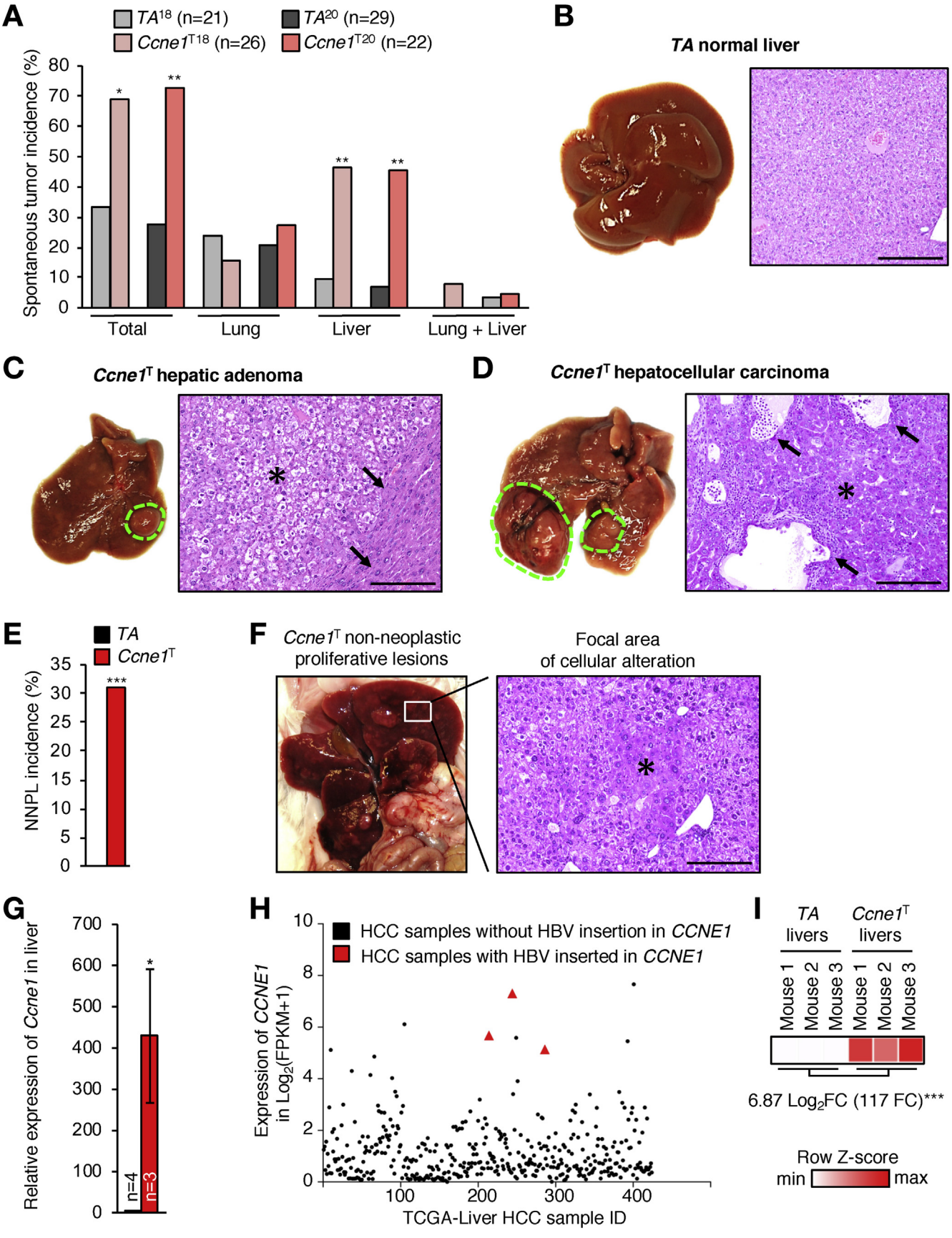
A
TA18 (n=21)
TA20 (n=29)
Ccne1T18 (n=26)
Ccne1T20 (n=22)
Spontaneous tumor incidence (%)
Total
Lung
Liver
Lung + Liver
B
TA normal liver
C
Ccne1T hepatic adenoma
D
Ccne1T hepatocellular carcinoma
E
TA
Ccne1T
NNPL incidence (%)
F
Ccne1T non-neoplastic proliferative lesions
Focal area of cellular alteration
G
Relative expression of Ccne1 in liver
n=4
n=3
H
HCC samples without HBV insertion in CCNE1
HCC samples with HBV inserted in CCNE1
Expression of CCNE1 in Log2(FPKM+1)
TCGA-Liver HCC sample ID
I
TA livers
Ccne1T livers
Mouse 1
Mouse 2
Mouse 3
6.87 Log2FC (117 FC)***
Row Z-score
min
max

the previously discussed data reveal that cyclin E1 overexpression disrupts cell-cycle control and causes CIN in MEFs.

Ubiquitous Cyclin E1 Overexpression Selectively Induces Tumors in Liver

To assess the impact of cyclin E1 overexpression on tumorigenesis, we generated cohorts of *Ccne1*^{T18}, *Ccne1*^{T20}, and *TA* control mice that were on dox-containing water from 3 weeks (weaning) onward. These mice were killed and screened for tumors at 14 months of age. Tumors were collected and subjected to histopathological evaluation. Both *Ccne1* transgenic lines showed a dramatic increase in tumor incidence, which was solely driven by a strong predisposition for liver tumors (Figure 4*A*). Eight of 22 liver tumors that we evaluated were HCCs, and the remaining lesions were hepatic adenomas (Figure 4*B*–*D*). Furthermore, non-neoplastic proliferative lesions that are thought to be pre-neoplastic[29] were frequently observed in *Ccne1*^{T} livers, but not in *TA* control livers (Figure 4*E* and *F*). Taken together, these data demonstrate that high cyclin E1 overexpression selectively drives neoplastic growth of mouse hepatocytes. Importantly, these data further imply that high overexpression of cyclin E1 in HCCs of patients chronically infected with HBV or AAV2 with viral integrations in the *CCNE1* locus might be disease causing.

To determine the extent to which *Ccne1*^{T} represents a faithful model for these patients, we assessed whether levels of *CCNE1* overexpression reported in HCC samples with HBV or AAV2 integrations were similar to those seen in livers of dox-treated *Ccne1*^{T} mice. Three HCC samples with AAV2 insertions on average have 470-fold higher *CCNE1* transcript levels than normal liver tissue without viral integrations, as assessed by reverse-transcriptase quantitative polymerase chain reaction.[17] Using a similar approach, we found that livers of 4-month-old *Ccne1*^{T} mice had 428-fold higher *Ccne1* transcript levels than those of age-matched *TA* control mice (Figure 4*G*). Using RNA sequencing, we determined that *CCNE1* transcript levels of 3 HCC samples with HBV integrations in *CCNE1* ranked second, fourth, and seventh among 424 HCC samples in the TCGA cohort (Figure 4*H*). On average, these 3 tumors had 32-fold higher transcript levels than corresponding tumors without such insertions. RNA sequencing on livers of 4-month-old *Ccne1*^{T} and *TA* control mice revealed a 117-fold increase in *Ccne1* transcript levels of transgenic livers (Figure 4*I*). Collectively, these data indicate that our *Ccne1*^{T} transgenic mice constitute a reasonably faithful model for HCC tumors with AAV2 or HBV insertions.

Cyclin E1 Overexpression Causes Near Polyploid Aneuploidy in the Liver

To understand the mechanism(s) by which cyclin E1 overexpression promotes neoplastic transformation in hepatocytes, we characterized the impact of transgene induction at 3 weeks (the age we started dox treatment in our tumor susceptibility study) on genomic content, and numerical and structural chromosome integrity in these cells. Mouse hepatocytes remain in a proliferative mode during the first few weeks of postnatal life and then exit the cell cycle to become quiescent, a process that is largely completed by 4 weeks of age. At this point, quiescent hepatocytes are mononuclear with 2n or 4n DNA content, or binucleated with 2 × 2n DNA content.[30]

As expected, 5-week-old *TA* control mice that we treated with dox for 2 weeks after weaning showed a marked reduction in proliferating cells compared with 3-week-old mice, as evidenced by both staining for the mitotic marker phospho-histone H3^{Ser10} and EdU incorporation (Figure 5*A* and *B*). In contrast, dox-treated *Ccne1*^{T} counterparts sustained rates of hepatic cell division characteristic to the proliferative phase of postnatal liver development. In animals treated with dox for 2 weeks starting at 5 weeks of age, after cells had entered the quiescent phase, cyclin E1 overexpression also significantly increased hepatic cell proliferation, albeit to a lesser extent than from 3 to 5 weeks (Figure 5*A* and *B*). Furthermore, although hepatic cell proliferation rates in *Ccne1*^{T} mice treated with dox between 3 and 16 weeks of age remained significantly elevated over *TA* control mice, they were much lower than those observed between weeks 3 and 5 (Figure 5*A* and *B*). Collectively, these findings indicate that cyclin E1 overexpression increases hepatic cell proliferation irrespective of the timing of transgene induction. Cyclin E1 overexpression significantly decreased the proportion of binucleated hepatocytes, a finding that is indicative of cellular stress (Figure 5*C*).

Hepatocyte nuclear diameter measurements showed that cyclin E1 overexpression markedly increased nuclear size, regardless of whether transgene induction occurred during the proliferative or quiescence phase of liver development (Figure 5*D*). Comparison of *Ccne1*^{T} mice treated with dox for 2 or 13 weeks starting at 3 weeks of age indicated that this nuclear enlargement phenotype was progressive, at least in a subset of mice (Figure 5*D*). Hepatic

Figure 4. Cyclin E1 overexpression selectively induces tumors in liver. (*A*) Spontaneous tumor incidence in 14-month-old mice induced with dox from weaning (organs not included did not have noteworthy tumor incidence). (*B*) Gross image and histology of a 14-month-old *TA* liver. (*C*) Gross image and histology of a *Ccne1*^{T} hepatocellular adenoma (*), with loss of normal lobular architecture and irregular growth pattern, compressing the surrounding liver parenchyma (*arrows*). (*D*) Gross image and histology of a *Ccne1*^{T} hepatocellular carcinoma, with trabecular (*) and adenoid growth pattern and cystic dilation of the adenoid structures (*arrows*). (*E*) Incidence of non-neoplastic proliferative lesion (NNPL). (*F*) Gross image and histology of a *Ccne1*^{T} liver with a focal area of cellular alteration (*). (*G*) Reverse-transcriptase quantitative polymerase chain reaction analysis of *Ccne1* transcripts in 4-month-old livers of indicted genotypes. Data represent mean ± SEM. (*H*) RNA sequencing–based expression values of *CCNE1* in the indicated HCC samples of the TCGA cohort. (*I*) RNA sequencing–based *Ccne1* expression values for the indicated 4-month-old mouse livers. FC, fold change. Statistics: (*A*) and (*E*) 2-tailed Fisher's exact test; (*G*) 2-tailed unpaired *t* test. *$P < .05$, **$P < .01$, ***$P < .001$. Scale bars, 1 mm (*B*–*D*) and 300 μm (*F*).

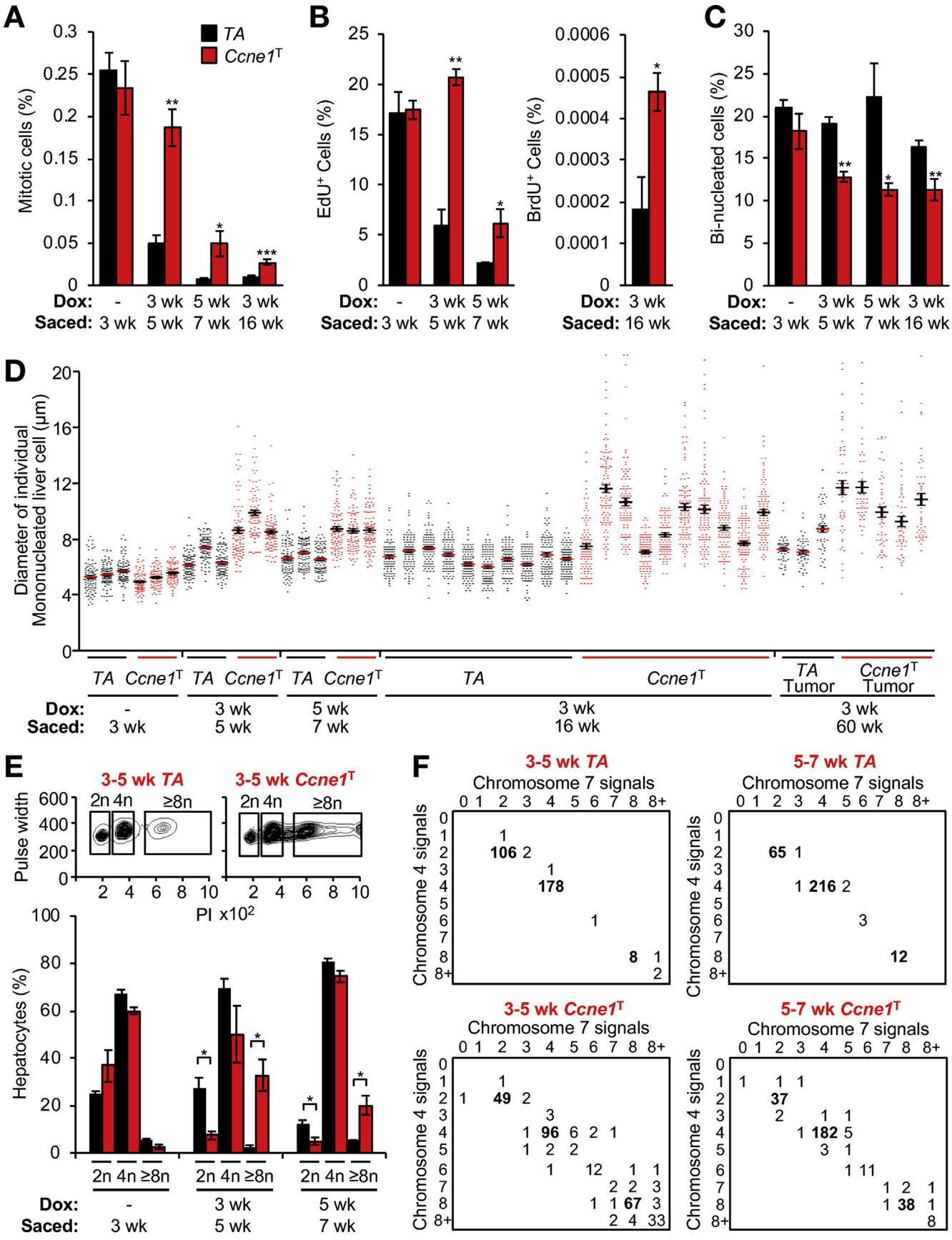

BASIC AND TRANSLATIONAL LIVER

tumors collected from 14-month-old dox-treated *Ccne1*^{T} mice had a very similar nuclear enlargement phenotype as livers from 4-month-old dox-treated *Ccne1*^{T} mice (Figure 5*D*). Nuclear size enlargement was not commonly observed in liver tumors from 14-month-old dox-treated *TA* mice (Figure 5*D*). FACS analysis of hepatocyte suspensions demonstrated that nuclear size enlargement with cyclin E1 overexpression is caused by polyploidization, irrespective of whether transgene induction occurs during the proliferative or quiescent phase of liver development (Figure 5*E*). FISH analysis of these same suspensions revealed that cyclin E1-induced polyploidization is frequently accompanied by aneuploidization (Figure 5*F,* Supplementary Figure 5*A*). FISH analysis on cell suspensions of other tissues from cyclin E1 overexpressing mice, including kidney, lung, and spleen, uncovered no evidence for polyploidization, although kidney and lung were prone to near-diploid aneuploidy (Supplementary Figure 5*B* and *C*). BrdU incorporation experiments confirmed that cyclin E1 overexpression increased cell proliferation in kidney and spleen (Supplementary Figure 5*D*). Collectively, these findings indicate that cyclin E1 overexpression promotes hepatocyte proliferation, polyploidization, and aneuploidization.

High Cyclin E1 Causes Chromosome Missegregation and DSBs in Hepatocytes

Next, we examined the extent to which the CIN phenotype observed in cyclin E1 overexpressing MEFs is conserved in hepatocytes. First, we immunolabeled liver sections from dox-treated *Ccne1*^{T} and *TA* mice for phospho-histone H3^{Ser10} and inspected mitotic figures for aberrantly arranged chromosomes. Chromosome misalignment outside of the metaphase plate was markedly increased in hepatic cells overexpressing cyclin E1, regardless of the timing of transgene induction (Figure 6*A*). We also observed a trend toward increased chromosome lagging, but anaphases were hard to find and values did not reach statistical significance. However, with the application of partial hepatectomy to stimulate cell division, we observed a high incidence of anaphases with lagging chromosomes on cyclin E1 overexpression (Figure 6*B*). Importantly, this correlated with high rates of nonperpendicular spindles (Figure 6*C*), which are enriched in merotelic microtubule-kinetochore attachments that produce lagging chromosomes.[26] Missegregation of whole chromosomes due to cyclin E1 overexpression was confirmed by single-cell genomic DNA sequencing on FACS-sorted hepatocytes with 4n DNA content (Figure 6*D* and *E*). Furthermore, focal amplifications and losses of chromosome segments were significantly increased with cyclin E1 overexpression (Figure 6*D* and *F*).

Segmental chromosome rearrangements require DSBs, which prompted us to determine whether this form of DNA damage was also increased in hepatocytes overexpressing cyclin E1. Indeed, immunolabeling of liver sections for γH2AX revealed that cyclin E1 overexpression significantly increased DSB formation, regardless of the timing of transgene induction (Figure 6*G*). The increase in DSBs did not appear to be simply the result of a higher ploidy status, and was selective for liver (Supplementary Figure 6*A*). Consistent with our observations in MEFs, elevated cyclin E1 levels in liver resulted in a reduction of Mcm2 in cytoplasmic, nuclear, and chromatin fractions, indicative of replication stress (Figure 6*H*). No such declines were observed in lung, kidney, and spleen, all of which failed to show evidence for increased DSBs (Figure 6*H*, and Supplementary Figure 6*B*).

High Cyclin E1 Induces Extensive Transcriptional Changes Selectively in Liver

To better understand why cyclin E1 overexpression selectively promotes liver tumorigenesis, we conducted genome-wide transcriptome profiling on liver, kidney, and lung samples of 4-month-old dox-treated *Ccne1*^{T} and *TA* mice. Hierarchical clustering based on gene expression pattern similarity grouped liver samples by genotype, but not kidney and lung samples (Figure 7*A*). In liver, cyclin E1 overexpression induced widespread transcriptional changes, with 2469 transcripts up-regulated and 2496 transcripts down-regulated (Figure 7*B*). In contrast, cyclin E1 overexpression altered <100 genes in kidney and lung (Figure 7*B*), even though the extent of *Ccne1* expression was similar in all 3 tissues (Supplementary Figure 7*A*). Using functional annotation analyses on the up-regulated differentially expressed genes, we identified hundreds of significantly enriched annotations in cyclin E1 overexpressing livers. We classified these into functional clusters (Figure 7*C*, Supplementary Figure 7*B* and *C*). One cluster indicated that overexpression of cyclin E1 increases oxidative phosphorylation (Figure 7*D*), in turn leading to oxidative stress (Figure 7*E*), a key feature of various human liver diseases, including HCC.[31–33] Staining of livers from 4-month-old mice with the reactive oxygen species–sensitive dye dihydroethidium (DHE) validated that cyclin E1 overexpression creates oxidative stress in the liver (Figure 7*F*).

Figure 5. Cyclin E1 overexpression causes near-polyploid aneuploidy in the liver. (*A*) Quantification of mitotic cells in liver sections immunostained with phospho-histone H3^{Ser10} (pHH3) (n = 3 per group except for the 3- to 16-week group in which n = 10 per group). (*B*) Quantification of EdU or BrdU-positive cells in liver sections of the indicated mice (n = 3 per group except for the 3- to 16-week group in which n = 11 per group). (*C*) Quantification of binucleated hepatocytes in liver sections stained with hematoxylin-eosin (n = 3 per group except for the 3- to 16-week group in which n = 10 per group; n = 200 hepatocytes per group). (*D*) Hepatocyte diameters in the indicated liver or liver tumor samples (each column represents 1 liver or liver tumor; n = 200 hepatocytes per sample). (*E*) *Top*: Flow cytometry profiles of hepatocyte ploidy as assessed by propidium iodide (PI) staining. *Bottom*: Quantification of hepatocyte DNA contents into diploid (2n), tetraploid (4n), and polyploid (≥8n) cell fractions (n = 3 mice per group). (*F*) FISH analysis for chromosome 4 and 7 signals on the hepatocyte suspensions used in (*E*) (n = 3 per group; n = 100 hepatocytes per sample). Data represent mean ± SEM. Statistics: (*A–E*) 2-tailed unpaired *t* test. **P* < .05, ***P* < .01, ****P* < .001.

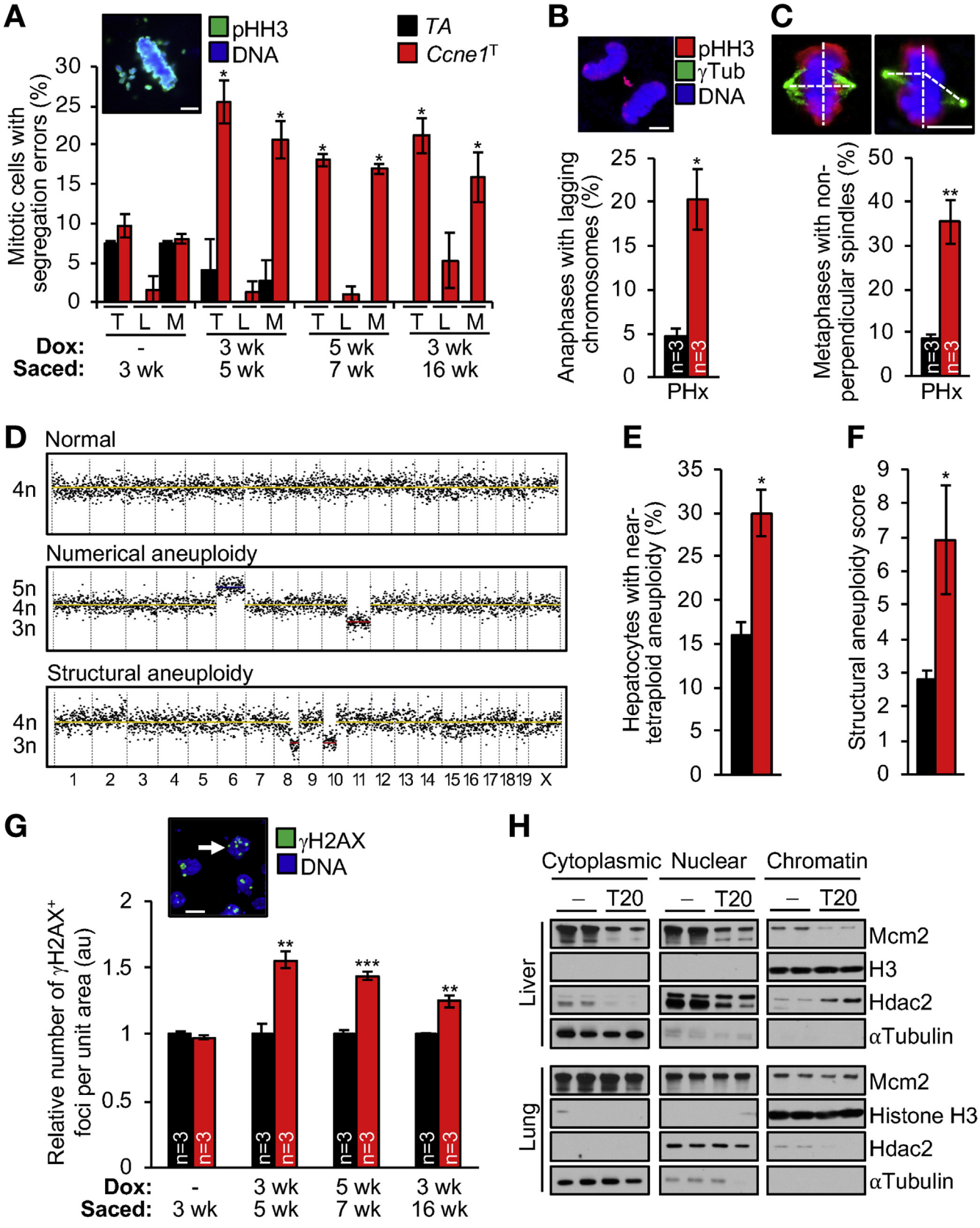
A
pHH3
DNA
TA
Ccne1T
Mitotic cells with segregation errors (%)
T L M
Dox: - 3 wk 5 wk 3 wk
Saced: 3 wk 5 wk 7 wk 16 wk
B
pHH3
γTub
DNA
Anaphases with lagging chromosomes (%)
PHx
C
Metaphases with non-perpendicular spindles (%)
PHx
D
Normal
4n
Numerical aneuploidy
5n
4n
3n
Structural aneuploidy
4n
3n
1 2 3 4 5 6 7 8 9 10 11 12 13 14 15 16 17 18 19 X
E
Hepatocytes with near-tetraploid aneuploidy (%)
F
Structural aneuploidy score
G
γH2AX
DNA
Relative number of γH2AX+ foci per unit area (au)
Dox: - 3 wk 5 wk 3 wk
Saced: 3 wk 5 wk 7 wk 16 wk
H
Cytoplasmic Nuclear Chromatin
– T20 – T20 – T20
Liver
Mcm2
H3
Hdac2
αTubulin
Lung
Mcm2
Histone H3
Hdac2
αTubulin

A second cluster identified by functional annotation analyses showed enrichment for immune system–related functions, including the up-regulation of multiple factors that regulate Tnf signaling (Figure 7*G*). Consistent with this, *Ccne1*^{T} livers showed elevated expression of *Tnf* (encoding Tnfα; Figure 7*G*), a cytokine linked to inflammation, necrosis, and apoptosis in various liver diseases, including HCC.[33–35] Kupffer cells were a source of increased Tnfα production, as evidenced by immunolabeling of liver sections from 4-month-old dox-treated *Ccne1*^{T} and *TA* mice for F4/80 and Tnfα (Figure 7*H*). Kupffer/macrophage cell numbers were not increased, and there was no evidence for an invasion of other immune cell types at 4 months (Supplementary Figure 7*D* and *E*).

Other clusters identified by functional annotation analyses showed enrichment for functions related to DNA damage/repair, p53 signaling, and cell death/survival (Figure 7*C*). All these clusters included several p53-regulated genes, including the cell-cycle regulators *Cdkn1a*, *Cdkn1b*, *Ccna2*, and *Ccnb1* (Figure 7*I*), the proapoptotic genes *Bbc3* (encoding Puma), *Bax*, and *Tnfrsf10* (encoding DR5/Killer) (Figure 7*J* and Supplementary Figure 8*A*), and the repair gene *Ddb2* (Supplementary Figure 8*B*). Western blot analysis of lysates of 4-month-old *Ccne1*^{T} and *TA* liver samples demonstrated that p53, p21, Bax, and Puma protein levels were up-regulated with cyclin E1 overexpression (Figure 7*K*). In contrast, p53 was consistently undetectable in *Ccne1*^{T} liver tumors (Figure 7*K*), indicating that inactivation of this tumor suppressor is a requirement for liver tumorigenesis in our model, which also holds true for many human HCCs.[36,37] Interestingly, although loss of p53 in *Ccne1*^{T} liver tumors coincided with reduced p21 expression, levels of Bax and Puma did not decline, implying that their expression was regulated in a p53-independent fashion (Figure 7*K*). Despite elevated expression of proapoptotic genes in 4-month-old *Ccne1*^{T} livers, cyclin E1 overexpression did not increase apoptosis, as revealed by terminal deoxynucleotidyl transferase–mediated deoxyuridine triphosphate nick-end labeling (TUNEL) staining (Figure 7*L*). Several genes associated with prosurvival functions were differentially up-regulated in 4-month-old *Ccne1*^{T} livers, including *Birc5*, which encodes Survivin (Figure 7*J* and Supplementary Figure 7*G*), raising the possibility that prosurvival mechanisms counteract proapoptotic functions to retain hepatocyte viability.

Induction of p21, as observed in 4-month-old *Ccne1*^{T} livers, is a feature of cellular senescence. Another key senescence marker, p16 (*Cdkn2a*), was, however, undetectable by RNA sequencing of these livers (data not shown). The same was true for key components of the senescence-associated secretory phenotype (Supplementary Figure 8*C*). In addition, 4-month-old *Ccne1*^{T} livers failed to stain for senescence-associated β-galactosidase, a widely used marker of senescence (Supplementary Figure 8*D*). Collectively, these data demonstrate that hepatocytes are unlikely to activate the senescence program in response to cyclin E1 overexpression.

Discussion

Our approach of ubiquitously overexpressing cyclin E1 uncovered that this cyclin is particularly oncogenic in hepatocytes, a finding that has several important clinical implications. First, our data indicate that in a subset of patients with HCC with chronic HBV infection, neoplastic transformation is likely to be driven by genomic integration of the virus in the *CCNE1* locus. Thus, it is not only important to treat chronic HBV infection early to reduce the risk of cirrhosis, but also to limit genomic viral integration in *CCNE1* and perhaps other common integration sites encoding oncogenes with putative neoplastic properties in the liver, such as *TERT* and *KMT2B*.[11,13,14] Second, our findings imply that insertion of AAV2 into the *CCNE1* locus is a capable initiating event in patients with HCC.[17] Unlike patients with HBV, HCC cases with AAV2 insertions show no evidence of cirrhotic disease, reminiscent of cyclin E1–overexpressing mice.[17] Third, AAV-derived vectors are now widely used as gene delivery tools in clinical-stage experimental therapeutic strategies for various conditions, including lipoprotein lipase deficiency, Leber congenital amaurosis, and the bleeding disorder hemophilia B. Although these vehicles thus far appear to be safe in both preclinical and clinical settings, the observation that robust *CCNE1* expression is sufficient to drive HCC in otherwise wild-type mice warrants consideration of precautionary monitoring of patients receiving AAV-based therapies for indications of liver pathology, particularly when vectors are used that show tropism toward hepatocytes. For instance, frequent noninvasive testing, such as alpha fetoprotein, might be beneficial.

Figure 6. Cyclin E1 overexpression causes a complex CIN phenotype in hepatocytes. (*A*) Chromosome segregation errors (T, total, L, lagging, M, misaligned) in liver sections of the indicated mice (n = 3 per group except for the 3- to 16-week group in which n = 9 per group). *Inset*, representative image of a cell in metaphase with misaligned chromosomes. (*B*) Quantification of anaphases with lagging chromosome in liver sections of the indicated 8-week-old mice 48 hours after partial hepatectomy (PHx). Image shows a representative *Ccne1*^{T} hepatocyte with a lagging chromosome. (*C*) Quantification of metaphases with nonperpendicular spindles in samples described in (*B*). Images show metaphases with perpendicular (*left*) and nonperpendicular spindles (*right*). (*D*) Representative segmentation plots of single tetraploid liver nuclei with normal ploidy, numerical aneuploidy and structural aneuploidy. (*E*, *F*) Numerical and structural aneuploidy assessments by single-cell DNA sequencing of hepatocytes FACS-sorted for 4n DNA content (n = 4 mice per group, 15–22 hepatocytes per mouse). (*G*) Quantification of γH2AX foci per nuclear area in liver sections of the indicated mice. Image represents γH2AX staining for liver cryosections at 4 months of age (*arrow* indicates a hepatic cell with an abundance of γH2AX-positive foci). (*H*) Western blots of fractionated lysates of liver and lung tissue Histone H3, Hdac2, and αTubulin represent chromatin, nuclear, and cytoplasmic markers, respectively. Data represent mean ± SEM. Statistics: (*A*–*G*) 2-tailed unpaired *t* test. $^{*}P < .05$, $^{**}P < .01$, $^{***}P < .001$. Scale bars, 5 μm.

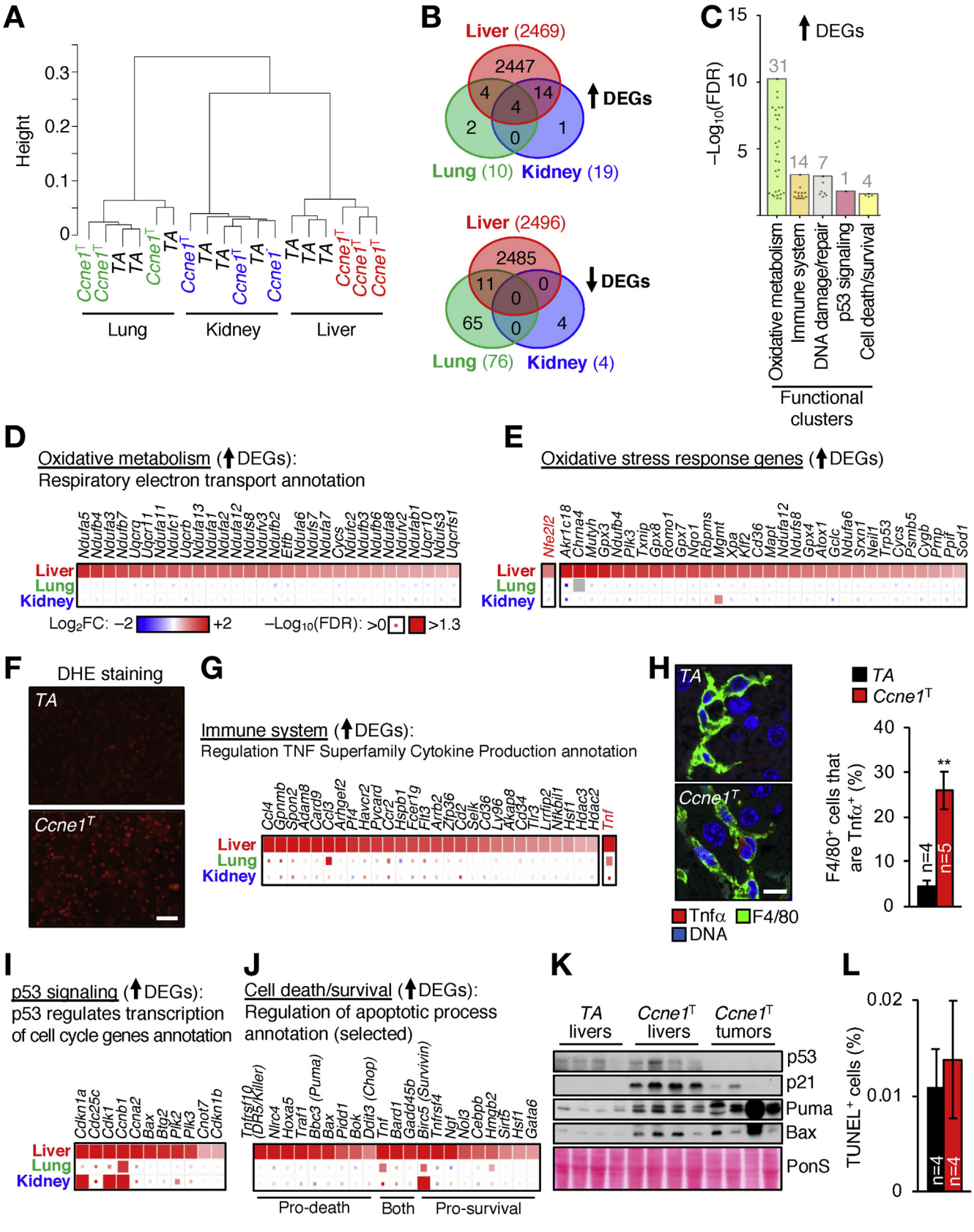
A
Height
0.3
0.2
0.1
0
Ccne1T
Ccne1T
TA
TA
Ccne1T
TA
Ccne1T
TA
TA
Ccne1T
TA
Ccne1
TA
TA
TA
Ccne1T
Ccne1T
Ccne1T
Lung
Kidney
Liver
B
Liver (2469)
2447
4
14
4
2
0
1
DEGs
Lung (10)
Kidney (19)
Liver (2496)
2485
11
0
0
65
0
4
DEGs
Lung (76)
Kidney (4)
C
15
10
5
−Log10(FDR)
DEGs
31
14
7
1
4
Oxidative metabolism
Immune system
DNA damage/repair
p53 signaling
Cell death/survival
Functional clusters
D
Oxidative metabolism (DEGs):
Respiratory electron transport annotation
Ndufa5 Ndufb4 Ndufa3 Ndufb7 Uqcrq Uqcr11 Ndufa11 Ndufc1 Uqcrb Ndufa13 Ndufa1 Ndufa2 Ndufa12 Ndufs8 Ndufv3 Ndufb2 Etfb Ndufa6 Ndufs7 Ndufa7 Cycs Ndufc2 Ndufb3 Ndufb6 Ndufa8 Ndufv2 Ndufab1 Uqcr10 Ndufs3 Uqcrfs1
Liver
Lung
Kidney
Log2FC: −2 +2
−Log10(FDR): >0 >1.3
E
Oxidative stress response genes (DEGs)
Nfe2l2 Akr1c18 Chrna4 Mutyh Gpx3 Ndufb4 Plk3 Txnip Gpx8 Romo1 Gpx7 Ngo1 Rbpms Mgmt Xpa Klf2 Cd36 Mapt Ndufa12 Ndufs8 Gpx4 Atox1 Gclc Ndufa6 Srxn1 Neil1 Trp53 Cycs Psmb5 Cygb Prnp Ppif Sod1
Liver
Lung
Kidney
F
DHE staining
TA
Ccne1T
G
Immune system (DEGs):
Regulation TNF Superfamily Cytokine Production annotation
Ccl4 Gpnmb Spon2 Adam8 Card9 Ccl3 Arhgef2 Pf4 Havcr2 Pycard Ccr2 Hspb1 Fcer1g Flt3 Arrb2 Zfp36 Cd2 Selk Cd36 Ly96 Akap8 Cd54 Tlr3 Lrrfip2 Nfkbil1 Hsf1 Hdac3 Hdac2 Tnf
Liver
Lung
Kidney
H
TA
Ccne1T
Tnfα F4/80
DNA
TA
Ccne1T
F4/80+ cells that are Tnfα+ (%)
40
30
20
10
0
**
n=4
n=5
I
p53 signaling (DEGs):
p53 regulates transcription of cell cycle genes annotation
Cdkn1a Cdc25c Cdk1 Ccnb1 Ccna2 Bax Btg2 Plk2 Plk3 Cnot7 Cdkn1b
Liver
Lung
Kidney
J
Cell death/survival (DEGs):
Regulation of apoptotic process annotation (selected)
Tnfsf10 (DR5/Killer) Nlrc4 Hoxa5 Traf1 Bbc3 (Puma) Bax Pidd1 Bok Ddit3 (Chop) Tnf Bard1 Gadd45b Birc5 (Survivin) Tnfrsf4 Ngf Nol3 Cebpb Hmgb2 Slrt5 Hsf1 Gata6
Pro-death
Both
Pro-survival
K
TA livers
Ccne1T livers
Ccne1T tumors
p53
p21
Puma
Bax
PonS
L
TUNEL+ cells (%)
0.02
0.01
0
n=4
n=4

Our studies provide insight into how and why cyclin E1 overexpression selectively drives tumorigenesis in the liver. Importantly, cyclin E1 overexpression increased aneuploidy in multiple tissues, but 2 other cancer-associated CIN phenotypes, polyploidization and DSBs, were observed only in hepatocytes. Our data suggest that cyclin E1 overexpression promotes polyploidization through precocious S-phase entry, erroneous DNA replication, and aberrant expression of mitotic regulators, resulting in abortion of mitotic progression and cytokinesis. Polyploidization may be further encouraged by compensatory proliferation in response to hepatocyte necrosis induced by Tnfα released by Kupffer cells.[32,33] Near polyploid-aneuploidies may arise when hepatocytes successfully separate their chromosomes but do so inaccurately due to aberrant centrosome dynamics, leading to merotely prone nonperpendicular spindles that yield lagging chromosomes. Our in-depth studies in MEFs suggest that cyclin E1 overexpression disrupts centrosome dynamics through hyperactivation of cyclin B2, Aurora A, and Plk1, 3 centrosome-associated core components of a signaling cascade that controls centrosome disjunction.[30,31,33] In addition to whole chromosome instability, we observed segmental aneuploidies, which are known to be induced by DSBs.[38] In MEFs, cyclin E1 overexpression induces replication stress, thus promoting the formation of chromatin bridges that resolve via DSBs.[30,39] Notably, transcriptomic analysis uncovered that cyclin E1 overexpressing hepatocytes experience oxidative stress, a well-documented alternative cause of DSBs.[39,40] In fact, given the rarity of chromatin bridges in anaphases on partial hepatectomy, oxidative stress may be the primary source of structural chromosome damage in hepatocytes that overexpress cyclin E1. Oxidative stress has been long recognized as a key contributor to the initiation and progression of cancer through multiple mechanisms, including oncogene activation, tumor suppressor gene inactivation, aberrant metabolism, and mitochondrial dysfunction.[41] p53 is activated in response to oxidative stress to remove damage to genomic and mitochondrial DNA and to regulate the expression of antioxidant genes,[42,43] and its inactivation is associated with tumor progression.[36,37,44] We consistently observed this exact pattern of activation of p53 at the preneoplastic stage and the subsequent inactivation of p53 as tumors emerge, giving credence to the idea that oxidative stress caused by cyclin E1 overexpression drives liver tumorigenesis.

In closing, our demonstration here that cyclin E1 overexpression causes liver-specific molecular and cellular defects underscores that it will be important to use comprehensive experimental approaches to assess whether and how overexpression of other genes at common integration sites of liver tropic viruses drives hepatocarcinogenesis. Such efforts hold promise for the identification of druggable molecular targets for the development of innovative experimental therapies for the treatment of HCC.

Supplementary Material

Note: To access the supplementary material accompanying this article, visit the online version of *Gastroenterology* at www.gastrojournal.org, and at https://doi.org/10.1053/j.gastro.2019.03.016.

References

1. Ohtsubo M, Roberts J. Cyclin-dependent regulation of G1 in mammalian fibroblasts. Science 1993;259:1908–1912.
2. Resnitzky D, Gossen M, Bujard H, et al. Acceleration of the G1/S phase transition by expression of cyclins D1 and E with an inducible system. Mol Cell Biol 1994;14:1669–1679.
3. Geng Y, Yu Q, Sicinska E, et al. Cyclin E ablation in the mouse. Cell 2003;114:431–443.
4. Parisi T, Beck AR, Rougier N, et al. Cyclins E1 and E2 are required for endoreplication in placental trophoblast giant cells. EMBO J 2003;22:4794–4803.
5. Geng Y, Michowski W, Chick JM, et al. Kinase-independent function of E-type cyclins in liver cancer. Proc Natl Acad Sci U S A 2018;115:1015–1020.
6. Geng Y, Lee Y-M, Welcker M, et al. Kinase-independent function of cyclin E. Mol Cell 2007;25:127–139.

Figure 7. Identification of protumorigenic changes in preneoplastic livers of mice overexpressing cyclin E1. (*A*) Hierarchical clustering using RNA sequencing data from lung, liver, and kidney of the indicated 4-month-old mice. The *y*-axis represents the metric 1-Pearson correlation as distance between samples. (*B*) Venn diagrams depicting numbers of significantly up- or down-regulated differentially expressed genes (DEGs) in the indicated *Ccne1*^{T} tissues versus corresponding *TA* tissues. (*C*) Selected functional clusters overrepresented in up-regulated DEGs from *Ccne1*^{T} vs *TA* livers. Points within each cluster represent individual annotations. The total number of annotations per cluster is indicated. FDR, false discovery rate. (*D*) Heatmap of up-regulated DEGs for the indicated annotation. Depicted are $\log_2$ fold expression changes in *Ccne1*^{T} vs *TA* tissues (box color) and the significance per gene (box size). (*E*) Heatmap of up-regulated DEGs generated from gene ontology annotation "Response to oxidative stress." (*F*) Representative images of cryo-sections of the indicated 4-month-old livers stained with dihydroethidium (DHE). Scale bar, 40 μm. (*G*) Heatmap of up-regulated DEGs for the indicated annotation within the immune system cluster. (*H*) *Left:* Images of representative liver sections of the indicated 4-month-old mice immunolabeled for Tnfα and F4/80. Scale bar, 10 μm. *Right:* Quantitation of Tnfα^{+} cells among the F4/80^{+} cells in the indicated liver sections. (*I*, *J*) Heatmaps of up-regulated DEGs for the indicated annotations of the "p53 signaling" and "cell/death/survival" clusters, respectively. (*K*) Western blots of lysates from 4-month-old livers and liver tumors of 14-month-old mice. Ponceau S (PonS) served as loading control. (*L*) Quantification of terminal deoxynucleotidyl transferase–mediated deoxyuridine triphosphate nick-end labeling (TUNEL)-positive cells in liver sections of the indicated 4-month-old mice. Data in (*H*) and (*L*) represent mean ± SEM. Statistics: (*H*) and (*L*) 2-tailed unpaired *t* test. $^{**}P < .01$. Heatmap legends in (*E*), (*G*), (*I*), and (*J*) are as in (*D*).

7. Ohashi R, Gao C, Miyazaki M, et al. Enhanced expression of cyclin E and cyclin A in human hepatocellular carcinomas. Anticancer Res 2001;21:657–662.
8. Bartkova J, Rezaei N, Liontos M, et al. Oncogene-induced senescence is part of the tumorigenesis barrier imposed by DNA damage checkpoints. Nature 2006; 444:633–637.
9. Spruck CH, Won KA, Reed SI. Deregulated cyclin E induces chromosome instability. Nature 1999;401:297–300.
10. Beroukhim R, Mermel CH, Porter D, et al. The landscape of somatic copy-number alteration across human cancers. Nature 2010;463:899.
11. Schulze K, Imbeaud S, Letouze E, et al. Exome sequencing of hepatocellular carcinomas identifies new mutational signatures and potential therapeutic targets. Nat Genet 2015;47:505–511.
12. Cancer Genome Atlas Network. Comprehensive and integrative genomic characterization of hepatocellular carcinoma. Cell 2017;169:1327–1341.e23.
13. Sung WK, Zheng H, Li S, et al. Genome-wide survey of recurrent HBV integration in hepatocellular carcinoma. Nat Genet 2012;44:765–769.
14. Zhao LH, Liu X, Yan HX, et al. Genomic and oncogenic preference of HBV integration in hepatocellular carcinoma. Nat Commun 2016;7:12992.
15. Purcell RH. The discovery of the hepatitis viruses. Gastroenterology 1993;104:955–963.
16. Calcedo R, Vandenberghe LH, Gao G, et al. Worldwide epidemiology of neutralizing antibodies to adeno-associated viruses. J Infect Dis 2009;199:381–390.
17. Nault JC, Datta S, Imbeaud S, et al. Recurrent AAV2-related insertional mutagenesis in human hepatocellular carcinomas. Nat Genet 2015;47:1187–1193.
18. Hochedlinger K, Yamada Y, Beard C, et al. Ectopic expression of Oct-4 blocks progenitor-cell differentiation and causes dysplasia in epithelial tissues. Cell 2005; 121:465–477.
19. Nam HJ, van Deursen JM. Cyclin B2 and p53 control proper timing of centrosome separation. Nat Cell Biol 2014;16:538–549.
20. Kahraman A, Barreyro FJ, Bronk SF, et al. TRAIL mediates liver injury by the innate immune system in the bile duct-ligated mouse. Hepatology 2008;47:1317–1330.
21. Mitchell C, Willenbring H. A reproducible and well-tolerated method for 2/3 partial hepatectomy in mice. Nat Protoc 2008;3:1167–1170.
22. van den Bos H, Bakker B, Taudt A, et al. Quantification of aneuploidy in mammalian systems. Methods Mol Biol 2019;1896:159–190.
23. Ricke RM, Jeganathan KB, Malureanu L, et al. Bub1 kinase activity drives error correction and mitotic checkpoint control but not tumor suppression. J Cell Biol 2012; 199:931–949.
24. Liu Q, Guntuku S, Cui XS, et al. Chk1 is an essential kinase that is regulated by Atr and required for the G(2)/M DNA damage checkpoint. Genes Dev 2000;14:1448–1459.
25. Ganem NJ, Godinho SA, Pellman D. A mechanism linking extra centrosomes to chromosomal instability. Nature 2009;460:278–282.
26. van Ree JH, Nam HJ, van Deursen JM. Mitotic kinase cascades orchestrating timely disjunction and movement of centrosomes maintain chromosomal stability and prevent cancer. Chromosome Res 2016;24:67–76.
27. Gregan J, Polakova S, Zhang L, et al. Merotelic kinetochore attachment: causes and effects. Trends Cell Biol 2011;21:374–381.
28. Ren B, Cam H, Takahashi Y, et al. E2F integrates cell cycle progression with DNA repair, replication, and G(2)/M checkpoints. Genes Dev 2002;16:245–256.
29. Iwasa J, Shimizu M, Shiraki M, et al. Dietary supplementation with branched-chain amino acids suppresses diethylnitrosamine-induced liver tumorigenesis in obese and diabetic C57BL/KsJ-db/db mice. Cancer Sci 2010; 101:460–467.
30. Wang MJ, Chen F, Lau JTY, et al. Hepatocyte polyploidization and its association with pathophysiological processes. Cell Death Dis 2017;8:e2805.
31. Satapati S, Kucejova B, Duarte JA, et al. Mitochondrial metabolism mediates oxidative stress and inflammation in fatty liver. J Clin Invest 2016;126:1605.
32. Sakurai T, He G, Matsuzawa A, et al. Hepatocyte necrosis induced by oxidative stress and IL-1 alpha release mediate carcinogen-induced compensatory proliferation and liver tumorigenesis. Cancer Cell 2008;14:156–165.
33. Maeda S, Kamata H, Luo JL, et al. IKKbeta couples hepatocyte death to cytokine-driven compensatory proliferation that promotes chemical hepatocarcinogenesis. Cell 2005;121:977–990.
34. Pikarsky E, Porat RM, Stein I, et al. NF-kappaB functions as a tumour promoter in inflammation-associated cancer. Nature 2004;431:461–466.
35. Kamata H, Honda S, Maeda S, et al. Reactive oxygen species promote TNFalpha-induced death and sustained JNK activation by inhibiting MAP kinase phosphatases. Cell 2005;120:649–661.
36. Ozturk M. p53 mutation in hepatocellular carcinoma after aflatoxin exposure. Lancet 1991;338:1356–1359.
37. McClendon AK, Dean JL, Ertel A, et al. RB and p53 cooperate to prevent liver tumorigenesis in response to tissue damage. Gastroenterology 2011;141:1439–1450.
38. Richardson C, Jasin M. Frequent chromosomal translocations induced by DNA double-strand breaks. Nature 2000;405:697–700.
39. Svilar D, Goellner EM, Almeida KH, et al. Base excision repair and lesion-dependent subpathways for repair of oxidative DNA damage. Antioxid Redox Signal 2011; 14:2491–2507.
40. Sharma V, Collins LB, Chen TH, et al. Oxidative stress at low levels can induce clustered DNA lesions leading to NHEJ mediated mutations. Oncotarget 2016;7:25377–25390.
41. Kalyanaraman B, Cheng G, Hardy M, et al. Teaching the basics of reactive oxygen species and their relevance to cancer biology: Mitochondrial reactive oxygen species detection, redox signaling, and targeted therapies. Redox Biol 2018;15:347–362.
42. Sablina AA, Budanov AV, Ilyinskaya GV, et al. The antioxidant function of the p53 tumor suppressor. Nat Med 2005;11:1306–1313.

43. Zhuang J, Wang PY, Huang X, et al. Mitochondrial disulfide relay mediates translocation of p53 and partitions its subcellular activity. Proc Natl Acad Sci U S A 2013; 110:17356–17361.
44. Solimini NL, Xu Q, Mermel CH, et al. Recurrent hemizygous deletions in cancers may optimize proliferative potential. Science 2012;337:104–109.

Received August 15, 2018. Accepted March 7, 2019.

Reprint requests
Address requests for reprints to: Jan M. van Deursen, PhD, Mayo Clinic, 200 First Street SW, Rochester, Minnesota 55905. e-mail: vandeursen.jan@mayo.edu; fax: (507) 284-3383.

Acknowledgments
We thank Dr Darren Baker and members of the van Deursen laboratory for helpful discussions, feedback, or help with methods. We thank Wei Zhou and Ming Li of the Mayo Clinic's Gene Knockout Mouse Core Facility for ES cell microinjection and chimera breeding, Dr Arun Kanakkanthara for performing DNA fiber assays, the Cytogenetics Core for FISH, and the Sequencing Core of the Medical Genomics Facility for RNA sequencing.

Author contributions: KA and EH conducted tumor susceptibility studies and experiments in MEFs. JFL performed CIN assessments on the liver with assistance of GN, ROFV, SB, and GG. IS conducted transcriptomic studies in collaboration with CZ and HL and followed up on functional annotation analyses with assistance of EJVD, JHVR, and BVDS. KJ designed and performed experiments and analyzed results. FF, HVDB, and DS conducted single-cell whole genome sequencing and analyzed the results. DRO, JAK, and LRR conducted bioinformatics analyses on TCGA samples. SYH and ADB conducted histopathological analyses. JMVD, KA, JFL, and IS wrote the manuscript with input from all authors. JMVD directed and supervised the study.

Conflicts of interest
The authors disclose no conflicts.

Funding
This work was supported by National Institutes of Health, United States grant R01 CA096985 and CA168709 to JMVD.

Supplementary Methods

Indirect Immunofluorescence on MEFs and Confocal Microscopy

Indirect immunofluorescence was carried out as previously described.[1] Primary MEFs were cultured in the presence or absence of dox for 72 hours. For total cyclin E1, p-CDK substrate, γH2AX, and 53BP1 staining, cells were fixed in phosphate-buffered saline (PBS)/3% paraformaldehyde (PFA) for 12 minutes at room temperature (RT), permeabilized in PBS/0.2% Triton X-100 for 10 minutes and blocked in PBS/1% bovine serum albumin for 30 minutes at RT. A laser-scanning microscope (LSM 510 or LSM 780; Carl Zeiss, Oberkochen, Germany) with an inverted microscope (Axiovert 100M; Zeiss) was used to analyze immunostained cells and capture images. Quantification of protein signals was carried out using ImageJ software (National Institutes of Health, Bethesda, MD). Confocal microscopy images were converted to 8-bit gray scale, cell edges were traced, and the mean pixel integrated density (arbitrary units) within the marked area was calculated. Intensity values for each cell-cycle phase were normalized to G_1 intensity value of -dox MEFs for each cell line separately.

For quantification of supernumerary centrosomes, Eg5 staining or spindle geometry analysis, cells were fixed in PBS/1% PFA for 5 minutes at RT followed by 10 minutes on ice-cold methanol. αTubulin was used to mark microtubules emanating from centrosomes that were stained with γTubulin. Only centrosomes with spindle fibers were counted. For spindle geometry analysis, serial optical sections were collected from γTubulin/αTubulin-stained MEFs using a laser-scanning microscope. After maximum intensity projection, ZEN software (Zeiss) was used to measure the angle between the spindle and the metaphase plate. Cells that had an acute angle between the spindle pole axis and the metaphase plate of less than 85° or greater than 95° were considered nonperpendicular. Ten to 15 cells were analyzed per MEF line.

G_2 cells were identified using rabbit anti-phospho-histone $H3^{Ser10}$ (pHH3) (1:1000, 06-570; Millipore, Bedford, MA), which selectively stains heterochromatin foci in G_2 phase. For centrosome distance measurements in G_2, cells were fixed in PHEM buffer (25 mM HEPES, 10 mM EGTA, 60 mM PIPES, and 2 mM $MgCl_2$ at pH 6.9) for 5 minutes followed by ice-cold methanol for 10 minutes and stained for pHH3/γTubulin/Hoechst. Images were taken by laser-scanning microscopy of cells with centrosomes in the same focal plane. The distance between centrosomes (γTubulin signals) was measured using ZEN software (Zeiss). For centrosome specific staining of HA, cyclin B2, phospho-Plk1, and phospho-Aurora, cells were fixed in PHEM buffer for 5 minutes, followed by ice-cold methanol for 10 minutes. Centrosome movement analysis in prophase cells was performed as previously described.[4] Ten to 15 cells were analyzed per MEF line.

All confocal microscopy images are representative of at least 3 independent experiments. Primary antibodies for immunostaining were as follows: rabbit anti-cyclin E1 (1:100, ab7959; Abcam, Cambridge, UK); rabbit anti-pCdk substrates (1:1,000, #9447; Cell Signaling Technology, Danvers, MA); mouse anti-phospho-Plk1 (1:250, #ab39068/clone 2A3; Abcam); rabbit anti-pAur (1:100, #2914; Cell Signaling); rabbit anti-cyclin B2 (1:200, #sc-22776; Santa Cruz, Dallas, TX); mouse or rabbit anti-γTubulin (1:300, #T6557/clone GTU-88 or #T5192; Sigma-Aldrich, St Louis, MO); rabbit anti-pHH3 (1:1,000, #06-570; Millipore), mouse anti-αTubulin (1:1000, #T9026/clone DM1A; Sigma-Aldrich); rabbit anti-53BP1 (1:500, #NB100-305; Novus Biologicals, Littleton, CO); rabbit anti-Eg5 (1:100, #TA301478; OriGene, Rockville, MD); human anti-centromeric antibody (1:100, #15-234-0001; Antibodies, Inc., Davis, CA); rabbit anti-RPA2 (1:200, #ab61184; Abcam); mouse anti-phospho-histone H2AX (1:500, #05-636; Millipore).

Immunolabeling of Tissue Sections

For visualizing mitotic cells in liver tissue, livers were fixed in formalin for 24 hours and processed for paraffin embedding, sectioning (5 μm) and immunostained with rabbit anti-pHH3 (1:1000, #06-570; Millipore), as previously described.[3] To quantify total number of nuclei per section, average number of nuclei from 3 nonoverlapping fields at ×20 were counted using ImageJ and using the frame size of the image, the average number of nuclei per μm^2 was determined (N). Using the frame size and a ×10 tile scan image of the entire tissue section, the area of the section was determined (T). The total number of nuclei were then calculated by multiplying N * T. Mitotic index was calculated by dividing the total number of pHH3-positive nuclei by the total number of nuclei per section. For visualizing DNA double-strand breaks, cryosections (5 μm) were obtained from optical coherence tomography embedded tissue specimens, air-dried at RT, and fixed in PBS/4% PFA for 12 minutes. Sections were washed 3 times in PBS and antigen retrieval was performed in sodium citrate buffer at 80°C for 1 hour. Slides were cooled and then washed 3 times in PBS before blocking with normal goat serum in PBS (0.1% Triton-X) for 1 hour. Samples were incubated with primary antibody (mouse anti-phospho histone H2AX, 1:500, #JBW-301, Millipore; rabbit anti-pHH3, 1:1000, #06-570, Millipore) in blocking buffer overnight. Slides were rinsed 3 times in PBS, incubated with appropriate Alexa-Fluor conjugated secondary antibodies (Molecular Probes, Eugene, OR) in blocking buffer for 1 hour, and rinsed again in PBS. To visualize nuclei, samples were incubated in Hoechst (1:1000 in PBS; Invitrogen, Carlsbad, CA) for 5 minutes and rinsed twice in PBS before mounting with Vectashield (#H-1000; Vector Biolabs, Burlingame, CA) and cover-slipping. Punctate nuclear foci were quantitated by confocal microscopy as described previously. Immune cells were visualized using the same procedure with following antibodies: rabbit, anti-F4/80 (1:250, #70076; Cell Signaling), rabbit, anti-Cd3e (1:100, #99940; Cell Signaling), mouse, anti-TNFα (1:50, #sc-52746; Santa Cruz). DNA fiber assays were performed as previously described.[2]

For visualizing mitotic spindles in liver tissue after partial hepatectomy, livers were fixed in PBS/4% PFA at

4 °C for 24 hours and processed for paraffin embedding and sectioning (5 μm). Immunofluorescence was performed as described[3] using mouse anti-γTubulin (1:300, #T6557/clone GTU-88; Sigma-Aldrich) and rabbit anti-pHH3 (1:1,000, #06-570; Millipore) primary antibodies. Immunohistochemistry was performed as previously described.[4]

EdU and BrdU Labeling Experiments

EdU was intraperitoneally injected daily at 50 mg/kg in 5% dimethyl sulfoxide/PBS for 5 consecutive days. Mice were killed 24 hours after the last injection. For visualizing EdU-positive cells, paraffin-embedded liver sections (5 μm) were permeabilized using 0.5% Triton X-100 in PBS for 20 minutes and stained using the Click-iT EdU Alexa-Fluor 488 Imaging Kit (Thermo Fisher, Waltham, MA) as per manufacturer's instructions. BrdU was injected intraperitoneally with 200 μL BrdU (10 mg/mL; Sigma) in PBS. Mice were killed 24 hours later. BrdU visualization was conducted according to the manufacturer's instructions (BrdU In-Situ Detection Kit, #550803; BD Biosciences, San Jose, CA). Percentages of EdU- or BrdU-positive cells were calculated by counting total number of EdU- or BrdU-positive nuclei in a section and dividing it by the total number of nuclei in that section, as used to quantify the mitotic index.

Dihydroethidium Staining

Super oxide was detected using the reactive oxygen species–sensitive dye DHE (dihydroethidium, #D1168; Invitrogen). Staining was performed as described.[5] Briefly, fresh cryosections (10 μm) of unfixed, frozen 4-month-old livers were incubated with 5 μM DHE for 30 minutes at 37°C in a humidified, dark chamber. Sections were washed twice with PBS, cover-slipped and immediately imaged with an Olympus light microscope (BX53; Tokyo, Japan).

TUNEL Staining

Terminal deoxynucleotidyl transferase–mediated deoxyuridine triphosphate nick-end labeling (TUNEL) staining was performed on paraffin-embedded liver sections (5 μm) according to the manufacturer's instructions (In Situ Cell Death Detection, #11684795910; Sigma-Aldrich). To quantify TUNEL-positive cells, sections were counterstained with Hoechst and the percentage of TUNEL-positive cells was determined from 3 nonoverlapping fields at ×20. At least 600 cells were counted per sample.

SA-β-Gal Staining

Senescence-associated-β-galactosidase (SA-β-Gal) staining was performed on fresh sections (10 μm) of unfixed, frozen 4-month-old livers according to the manufacturer's protocol (#9860S; Cell Signaling). Sections were stained for 24 hours, washed with PBS, cover-slipped and imaged with an Olympus light microscope (BX53).

Live-Cell Imaging

For chromosome missegregation analysis, chromosome movements of monomeric red fluorescent protein (mRFP)-H2B-positive primary MEFs progressing through an unchallenged mitosis were followed at interframe intervals of 2 minutes as previously described.[1] MEFs were seeded onto 35-mm glass bottom dishes (MatTek, Ashland, MA). All experiments were carried out using a microscope system (Axio Observer; Zeiss) with CO_2 Module S, TempModule S, Heating Unit XL S, a Plan Apo ×63 NA 1.4 oil differential interference contrast III objective (Zeiss), camera (AxioCam MRm; Zeiss) and AxioVision 4.6 software (Zeiss). Imaging medium was kept at 37 °C. For analysis of cell-cycle duration, *Ccne1*^{T18} and *Ccne1*^{T20} MEFs were cotransduced with mKO2–hCdt1(30/120)/pCSII-EF and mAG–hGeminin(1/110)/pCSII-EF lentiviruses[6] grown in the presence or absence of dox for 48 hours, and then followed by live-cell imaging for 72 hours. Time-lapse images of differential interference contrast, mCherry, and Venus fluorescent signals were captured every 5 minutes using a Plan Apochromat ×20/0.8 M27 $D = 0.55$ objective. Fluorescence intensity was quantified semi-automatically for each mCherry and Venus individual image using the mean region of interest (ROI) tool within the ZEN software. Specifically, a constant circular ROI was selected to encompass the cell of interest and the same ROI area size was used for background subtraction. The G_1/S time was defined as the time with the lowest Venus intensity. The S/G_2 time was defined as the time for which mCherry ends the high intensity plateau and begins a descending slope. Nuclear envelope breakdown (mitosis entry) was identified by differential interference contrast and by the diffusion of nuclear Venus into mitotic cytosol. Nocodazole challenge assay was performed as described.[1]

RNA Isolation and Quantitative Polymerase Chain Reaction

RNA extraction (RNeasy Mini kit, #74104 or RNeasy Micro kit, #74004; Qiagen, Valencia, CA), complementary DNA synthesis (SuperScript III First-Strand Synthesis System, #18080051; Invitrogen), and reverse-transcriptase quantitative polymerase chain reaction (RT-qPCR) analysis (SYBR Green Real-Time PCR Master Mix, #4309155; Applied Biosystems, Foster City, CA) were performed according to the manufactures' instructions. The on-column DNase digestion step was avoided during the RNA extraction procedure unless RNA was used for RNA sequencing purposes. *Hprt* was used as a reference gene for RT-qPCR analyses. Primer sequences used were: *Ccne1* Forward 5′-CTCCAGAAAAAGGAAGGCAA-3′; *Ccne1* Reverse 5′-TCCACGCATGCTGAATTATC-3′; *Hprt* Forward 5′-TCATGGACTGATTATGGACAGG-3′; *Hprt* Reverse 5′-AATCCAGCAGGTCAGCAAA-3′.

RNA Sequencing Library Preparation and Sequencing and Bioinformatic Analyses

RNA quality and quantity were assessed using Agilent Bioanalyzer RNA 6000 Pico chips (#5067-1513; Agilent Technologies, Santa Clara, CA). Approximately 200 ng high-quality RNA from liver, lung, and kidney samples were

subjected to library preparation using the TruSeq RNA Library Prep Kit v2 (#RS-122-2001; Illumina, San Diego, CA), according to manufacturer's instructions. The concentration and size distribution of the completed libraries were confirmed using Agilent DNA 1000 chips (#5067-1504; Agilent Technologies) and Qubit fluorometry (Qubit dsDNA HS, #Q32851; Invitrogen). Libraries were sequenced following Illumina's standard protocol using the Illumina cBot and HiSeq 3000/4000 PE Cluster Kit. Flow cells were sequenced as 100 $\times$ 2 paired-end reads on an Illumina HiSeq 4000 using HiSeq 3000/4000 sequencing kit and HCS 3.3.20 collection software. Base-calling was performed using Illumina's RTA 2.5.2 software. RNA sequencing was performed at the Mayo Clinic Center for Individualized Medicine Medical Genomics Facility (Mayo Clinic, Rochester, MN). Fastq files of paired-end reads were aligned with Tophat 2.0.14 to the UCSC reference genome mm10 using Bowtie2 2.2.6 with default parameters. Gene level counts were obtained using FeatureCounts 1.4.6 from the SubRead package with gene models from corresponding UCSC annotation packages. Differential expression analysis was performed using R package DESeq2 1.10.1 after removing genes with average raw counts less than 10. Datasets from liver, lung, and kidney tissue were analyzed separately, except for the direct comparison of *Ccne1* expression levels presented in Figure 4*I*, Figure 7*A*, and Supplementary Figure 7*A*. Differential expression results are summarized in Supplementary Table 2. Genes with false discovery rate < 0.05 and lfcMLE (unshrunk log2 fold change produced by DESeq2) $\geq +0.45$ or ≤ -0.45 were considered significantly up-regulated or down-regulated, respectively. Hierarchical clustering of samples was performed using DESeq2-normalized counts with 1-Pearson correlation as distance and average linkage using hclust function in R 3.2.3. The dendrogram was generated based on the gene expression profiles across all replicate. For functional annotation analysis, the Fisher's exact test was used to determine overrepresented functions/gene sets in significantly up- or down-regulated genes from the liver. Gene sets were described in Enrichment Map.[7] Functional clusters were defined manually. Functional annotation analysis results are summarized in Supplementary Table 3. Oxidative stress response genes were extracted from Gene Ontology Consortium and QuickGO database for the annotation GO:0006979 "Response to oxidative stress."[8] Gene lists from both reference databases were merged resulting in the identification of 199 genes. The key oxidative stress response transcription factor Nfe2l2/Nrf2 was added manually. The oxidative stress response gene list was compared with differentially up-regulated gene lists from *Ccne1*^{T} vs *TA* datasets. Heatmaps were generated with Morpheus, Broad Institute (https://software.broadinstitute.org/morpheus) using lfcMLE values and negative Log10 (false discovery rate) values.

TCGA Analysis

Three HCC samples (TCGA-ED-A7XO-01A-11R-A352-07, TCGA-DDAADV-01A-11R-A39D-07, and TCGA-DD-AACV-01A-11R-A41C-07) with HBV integration in the *CCNE1* locus were evaluated for *CCNE1* expression among 424 samples with *CCNE1* expression data available in the TCGA-Liver Hepatocellular carcinoma cohort.

Data Availability

RNA sequencing data have been deposited in the Gene Expression Omnibus under the accession number GSE126445.

References

1. Nam HJ, van Deursen JM. Cyclin B2 and p53 control proper timing of centrosome separation. Nat Cell Biol 2014;16:538–549.
2. Tammachote R, Hommerding CJ, Sinders RM, et al. Ciliary and centrosomal defects associated with mutation and depletion of the Meckel syndrome genes MKS1 and MKS3. Hum Mol Genet 2009;18:3311–3323.
2. van Ree JH, Nam HJ, Jeganathan KB, et al. Pten regulates spindle pole movement through Dlg1-mediated recruitment of Eg5 to centrosomes. Nat Cell Biol 2016;18:814–821.
3. Kanakkanthara A, Jeganathan KB, Limzerwala JF, et al. Cyclin A2 is an RNA binding protein that controls Mre11 mRNA translation. Science 2016;353:1549–1552.
5. Gentric G, Maillet V, Paradis V, et al. Oxidative stress promotes pathologic polyploidization in nonalcoholic fatty liver disease. J Clin Invest 2015;125:981–992.
6. Sakaue-Sawano A, Kurokawa H, Morimura T, et al. Visualizing spatiotemporal dynamics of multicellular cell-cycle progression. Cell 2008;132:487–498.
7. Merico D, Isserlin R, Stueker O, et al. Enrichment map: a network-based method for gene-set enrichment visualization and interpretation. PLoS One 2010;5:e13984.
8. The Gene Ontology Consortium. Expansion of the Gene Ontology knowledgebase and resources. Nucleic Acids Res 2017;45:D331–D338.

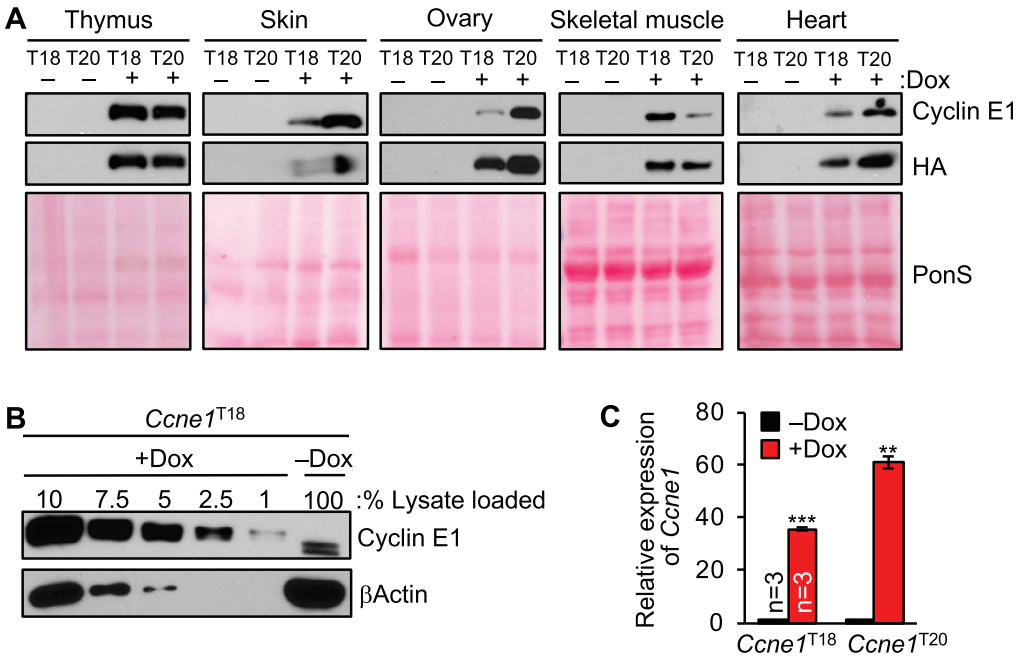

Supplementary Figure 1. *Ccne1*^{T} mice ubiquitously overexpress cyclin E1. (*A*) Western blots of tissue extracts from the indicated 6-week-old mice. Ponceau S (PonS) staining served as a loading control. (*B*) Western blot of serially diluted lysates of dox-treated *Ccne1*^{T18} MEFs and undiluted lysate of noninduced *Ccne1*^{T18} MEFs. (*C*) RT-qPCR analysis of *Ccne1* transcripts in MEFs cultured in the presence or absence of dox for 72 hours. Data represent mean ± SEM. Statistics: (*C*) 2-tailed paired *t* test. $^{**}P < .01$, $^{***}P < .001$.

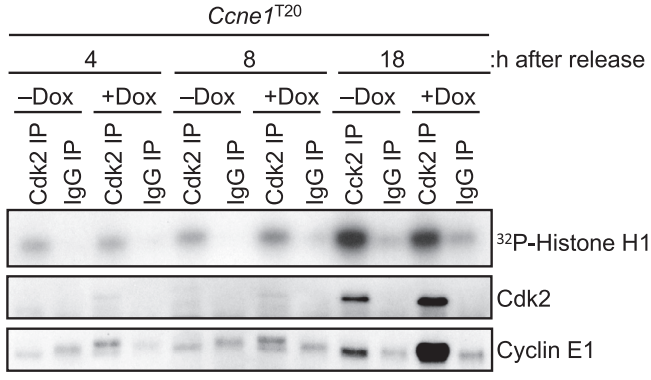

Supplementary Figure 2. Kinase assays measuring the catalytic activity of immunocomplexes precipitated with anti-Cdk2 antibody from dox-treated and untreated *Ccne1*^{T20} MEFs at various of the cell cycle. Histone 1 was used as substrate. Immunoglobulin (Ig)G immunocomplexes were used a negative control.

A

MEF line	Spreads inspected	% Aneuploidy	Karyotypes with indicated chromosome number											%PMSCS	% Breaks
			≤35	36	37	38	39	40	41	42	43	44	45		
Ccne1^{T18} –Dox	160	17	0	0	1	8	7	135	8	1	0	0	0	4	2
Ccne1^{T18} +Dox	150	40	0	2	6	8	13	90	18	12	1	0	0	4	7
Ccne1^{T20} –Dox	150	13	1	0	0	2	7	130	8	1	1	0	0	5 (2)	1 (1)
Ccne1^{T20} +Dox	150	27	0	2	0	6	17	109	13	2	1	0	0	8 (3)	13 (5)

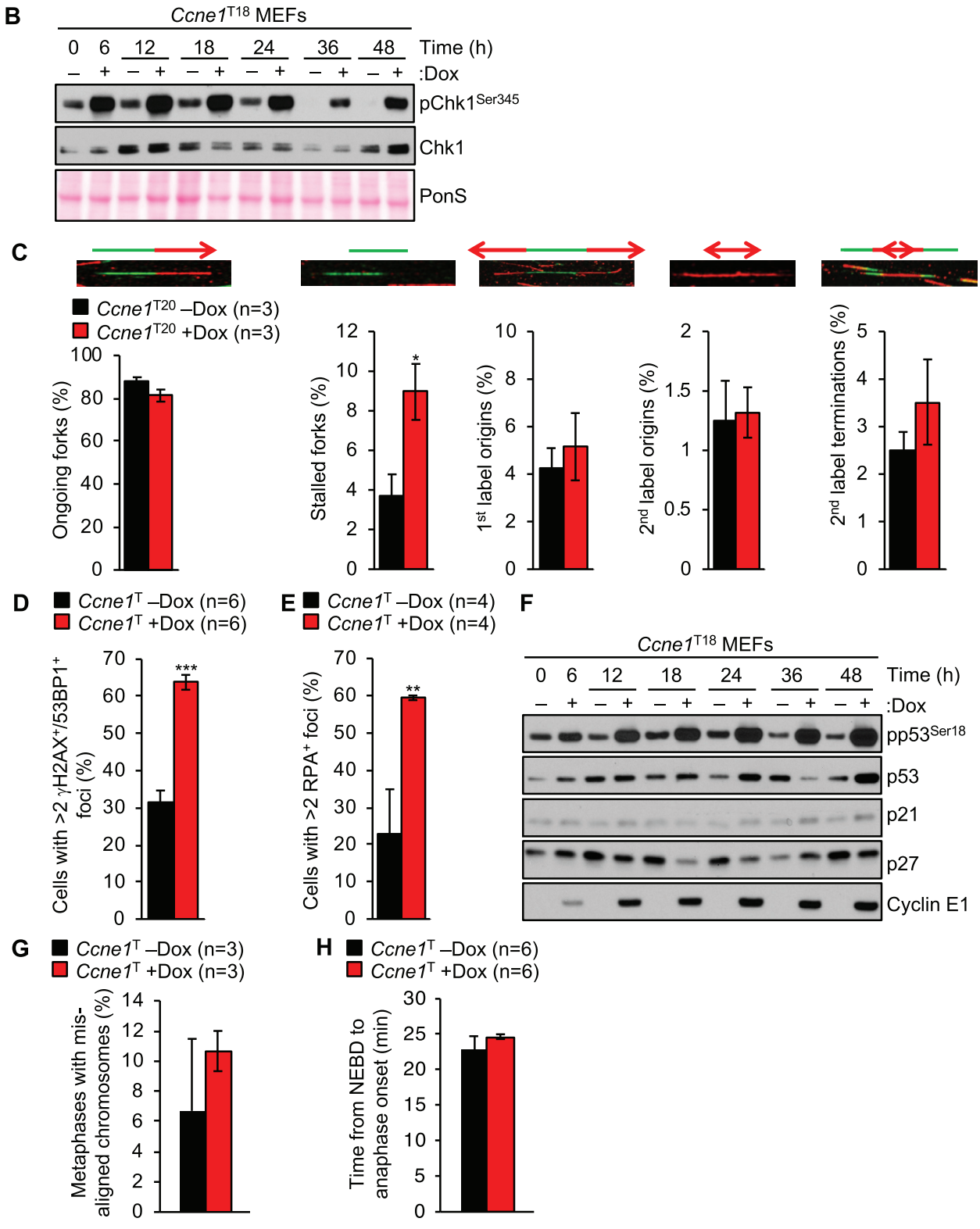

Supplementary Figure 3. Cyclin E1 overexpression causes replication stress. (*A*) Chromosome number distribution of the indicated MEFs. (*B*) Western blot analysis of MEF lysates at indicated time points after dox induction. (*C*) *Top*: Examples of replication defects characterized using DNA fiber assay. *Bottom*: Quantification of replication errors. (*D*) Quantification of DSBs using γH2AX and 53BP1 as markers. (*E*) Quantification of single-strand breaks by RPA2 immunostaining. (*F*) Western blots of the same MEF lysates shown in (*B*). (*G*) Incidence of misaligned chromosomes in MEFs after monastrol washout. (*H*) Time from nuclear envelop breakdown (NEBD) to anaphase onset in MEFs expressing H2B-mRFP. Data represents mean ± SEM. Statistics: (*C–H*) 2-tailed paired *t* test. $^{*}P < .05$, $^{**}P < .01$, $^{***}P < .001$.

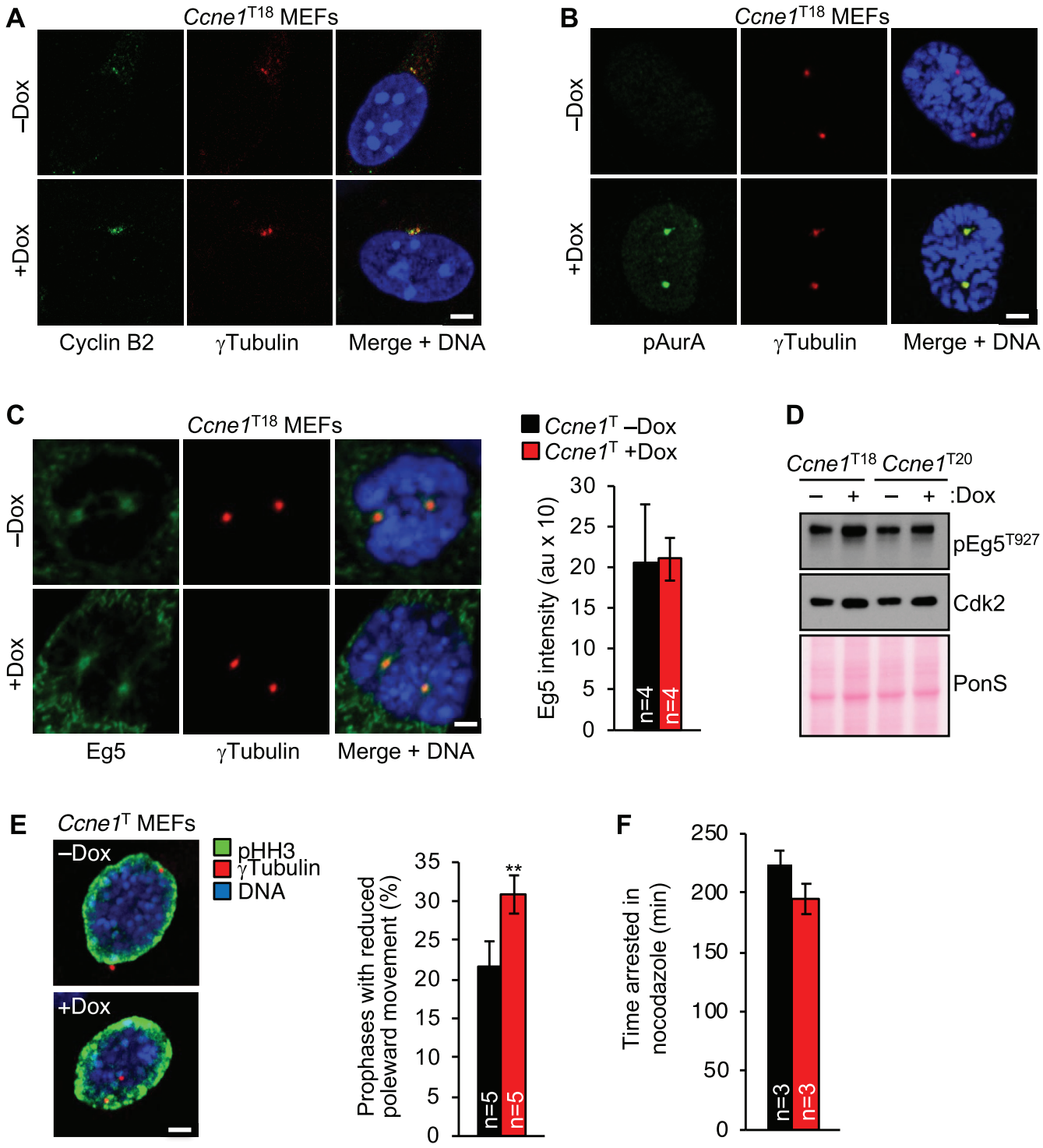

Supplementary Figure 4. Cyclin E1 overexpression causes premature activation of the cyclin B2-AurA-Plk1 signaling cascade that initiates centrosome disjunction. (*A*) Representative images of G_2 MEFs stained for cyclin B2 and γTubulin. (*B*) Representative prophases stained for pAurA and γTubulin. (*C*) Representative prophases (*left*) and quantification of Eg5 loading at the centrosome in prophase MEFs (*right*). (*D*) Western blots of lysates from mitotic shake-off MEFs. (*E*) Images illustrating reduced poleward movement of centrosomes in prophase with cyclin E1 overexpression (*left*) and quantitation of the defect (*right*). (*F*) Time spent in mitotic arrest for H2B-mRFP expressing *Ccne1*^{T18} MEFs challenged with nocodazole, determined by live cell imaging. Data represent mean ± SEM. Statistics: (*C*, *E*, *F*) 2-tailed paired *t* test. $^{**}P < .01$. Scale bars, 5 μm.

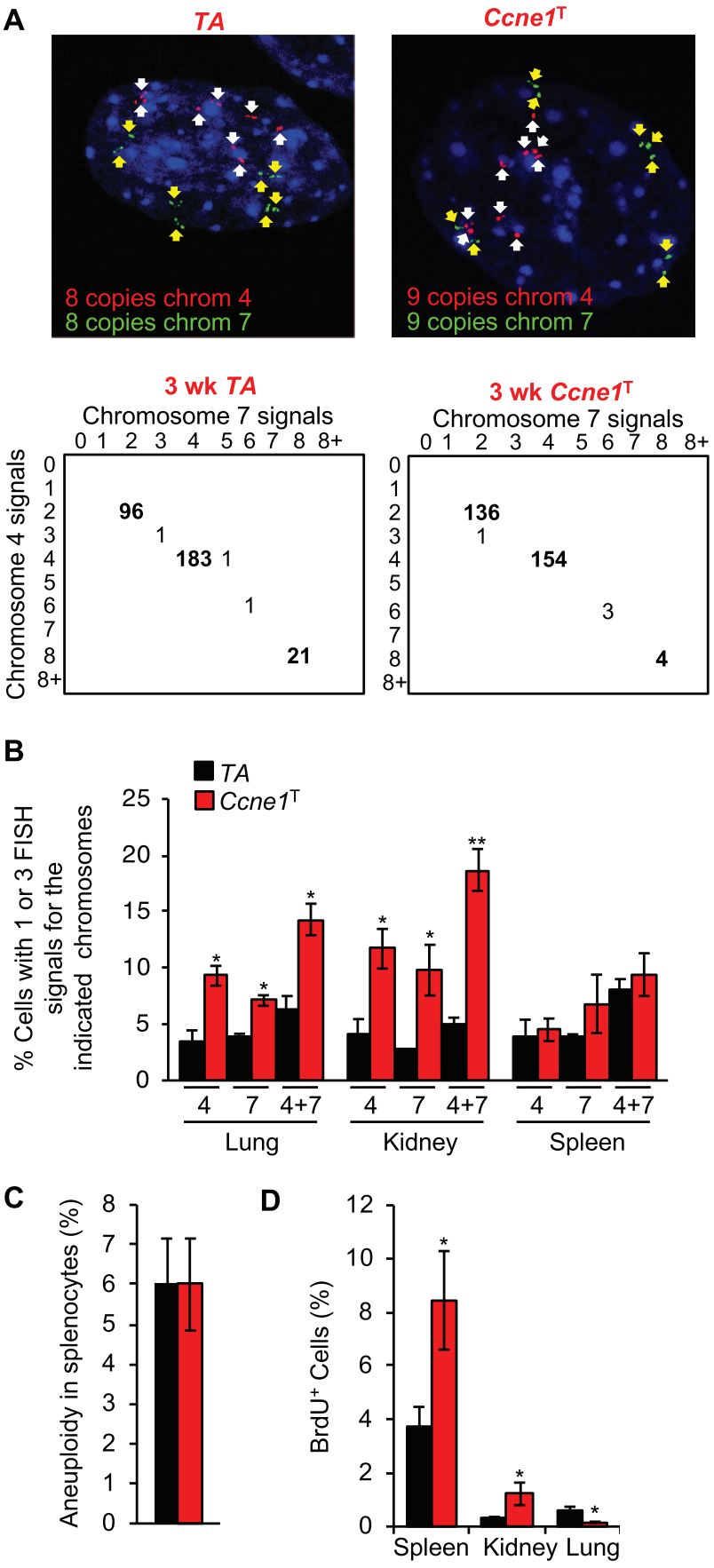

Supplementary Figure 5. Cyclin E1 overexpression causes aneuploidy in multiple tissues. (*A*) *Top*: Example of aneuploid and normal 8n hepatocytes. *Bottom*: FISH analysis for chromosome 4 and 7 signals on hepatocyte suspensions from 3-week-old mice (n = 3 per group, n = 100 hepatocytes per sample). (*B*) FISH analysis for chromosome 4 and 7 signals on indicated tissues from 4-month-old mice. (n = 3 to 6 animals per group, n = 100 cells per sample). We note that none of the samples contained polyploid cells (cells with 4 or 8 signals for both probes). (*C*) Chromosome counts on metaphase spreads of splenocytes from 5-month-old mice (n = 3 per group). (*D*) Quantification of BrdU-positive cells in tissue sections of 4-month-old mice (n = 9 per group). Data in (*B–D*) represent mean ± SEM. Statistics: (*B–D*) 2-tailed unpaired *t* test. $^{*}P < .05$, $^{**}P < .01$.

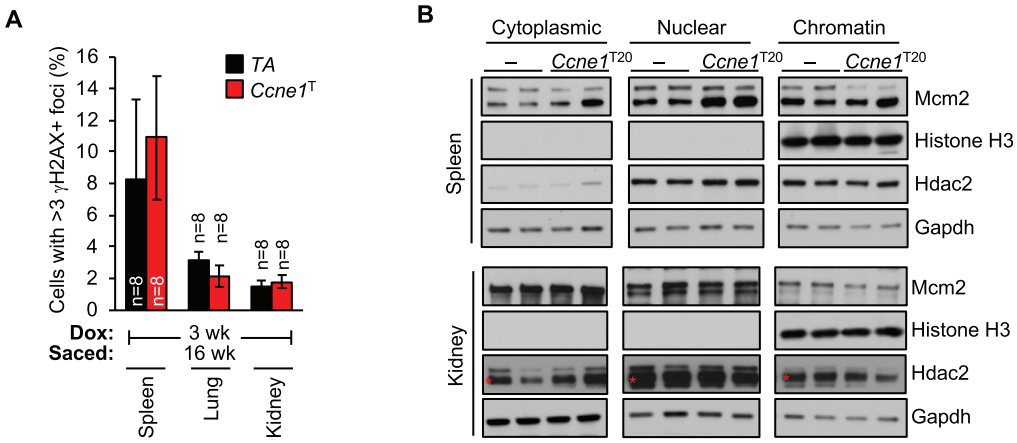

Supplementary Figure 6. DSBs and prereplication complex loading defects caused by cyclin E1 overexpression are liver specific. (*A*) Quantification of cells with >3 γH2AX foci in the indicated tissue sections (n = 3 mice per group). (*B*) Mcm2 subcellular distribution is normal in kidney and lung tissue of *Ccne1*^{T} mice. Western blots of fractionated tissue lysates. Histone H3, Hdac2, and Gapdh represent chromatin, nuclear, and cytoplasmic markers respectively. *Asterisks* denote a nonspecific band.

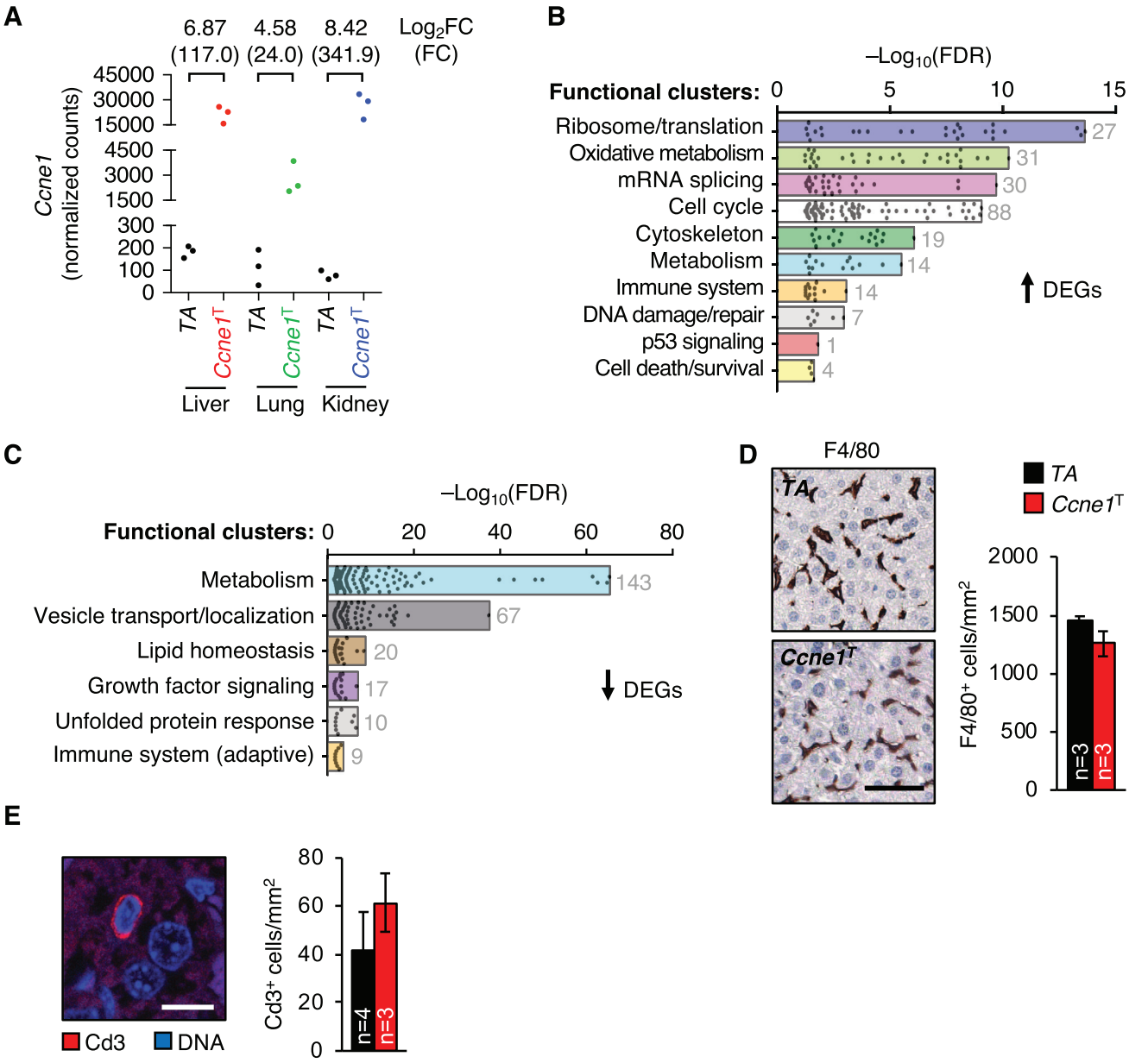

Supplementary Figure 7. Cyclin E1 overexpression impairs multiple signaling pathways in the liver. (*A*) *Ccne1* transcript levels quantified in RNA sequencing data. FC, fold change. (*B*, *C*) Complete list of functional clusters overrepresented in up-regulated (*B*) or down-regulated (*C*) differentially expressed genes (DEGs) from *Ccne1*^{T} vs *TA* livers. Points within each cluster represent individual annotations. The total number of annotations per cluster is indicated. FDR, false discovery rate. (*D*) Representative images (*left*) and quantification of immunohistochemistry for F4/80-positive macrophages in 4-month-old liver sections (*right*). Scale bar, 50 μm. (*E*) Representative images (*left*) and quantification of immunostaining for Cd3-positive T-cells in 4-month-old liver sections (*right*). Scale bar, 10 μm. Data in (*D*) and (*E*) represent mean ± SEM.

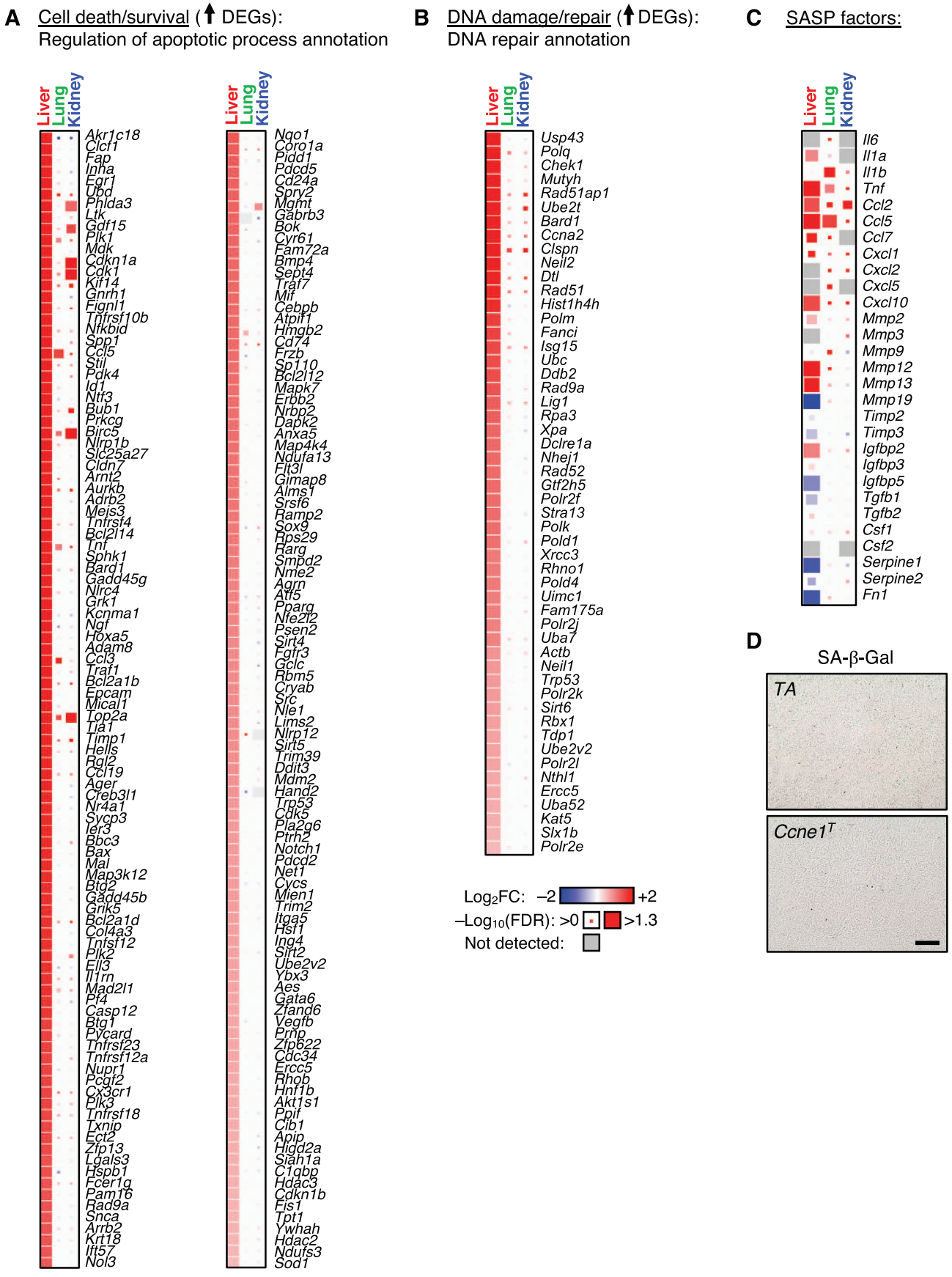
A
Cell death/survival (↑ DEGs):
Regulation of apoptotic process annotation
Liver
Lung
Kidney
Akr1c18
Clcf1
Fap
Inha
Egr1
Ubd
Phlda3
Ltk
Gdf15
Plk1
Mdk
Cdkn1a
Cdk1
Kif14
Gnrh1
Fignl1
Tnfrsf10b
Nfkbid
Spp1
Ccl5
Stil
Pdk4
Id1
Ntf3
Bub1
Prkcg
Birc5
Nlrp1b
Slc25a27
Cldn7
Arnt2
Aurkb
Adrb2
Meis3
Tnfrsf4
Bcl2l14
Tnf
Sphk1
Bard1
Gadd45g
Nlrc4
Grk1
Kcnma1
Ngf
Hoxa5
Adam8
Ccl3
Traf1
Bcl2a1b
Epcam
Mical1
Top2a
Tia1
Timp1
Hells
Rgl2
Ccl19
Ager
Creb3l1
Nr4a1
Sycp3
Ier3
Bbc3
Bax
Mal
Map3k12
Btg2
Gadd45b
Grik5
Bcl2a1d
Col4a3
Tnfsf12
Plk2
Ell3
Il1rn
Mad2l1
Pf4
Casp12
Btg1
Pycard
Tnfrsf23
Tnfrsf12a
Nupr1
Pcgf2
Cx3cr1
Plk3
Tnfrsf18
Txnip
Ect2
Zfp13
Lgals3
Hspb1
Fcer1g
Pam16
Rad9a
Snca
Arrb2
Krt18
Ift57
Nol3
Nqo1
Coro1a
Pidd1
Pdcd5
Cd24a
Spry2
Mgmt
Gabrb3
Bok
Cyr61
Fam72a
Bmp4
Sept4
Traf7
Mif
Cebpb
Atpif1
Hmgb2
Cd74
Frzb
Sp110
Bcl2l12
Mapk7
Erbb2
Nrbp2
Dapk2
Anxa5
Map4k4
Ndufa13
Flt3l
Gimap8
Alms1
Srsf6
Ramp2
Sox9
Rps29
Rarg
Smpd2
Nme2
Agrn
Atf5
Pparg
Nfe2l2
Psen2
Sirt4
Fgfr3
Gclc
Rbm5
Cryab
Src
Nle1
Lims2
Nlrp12
Sirt5
Trim39
Ddit3
Mdm2
Hand2
Trp53
Cdk5
Pla2g6
Ptrh2
Notch1
Pdcd2
Net1
Cycs
Mien1
Trim2
Itga5
Hsf1
Ing4
Sirt2
Ube2v2
Ybx3
Aes
Gata6
Zfand6
Vegfb
Prnp
Zfp622
Cdc34
Ercc5
Rhob
Hnf1b
Akt1s1
Ppif
Cib1
Apip
Higd2a
Stah1a
C1qbp
Hdac3
Cdkn1b
Fis1
Tpt1
Ywhah
Hdac2
Ndufs3
Sod1
B
DNA damage/repair (↑ DEGs):
DNA repair annotation
Liver
Lung
Kidney
Usp43
Polq
Chek1
Mutyh
Rad51ap1
Ube2t
Bard1
Ccna2
Clspn
Neil2
Dtl
Rad51
Hist1h4h
Polm
Fanci
Isg15
Ubc
Ddb2
Rad9a
Lig1
Rpa3
Xpa
Dclre1a
Nhej1
Rad52
Gtf2h5
Polr2f
Stra13
Polk
Pold1
Xrcc3
Rhno1
Pold4
Uimc1
Fam175a
Polr2j
Uba7
Actb
Neil1
Trp53
Polr2k
Sirt6
Rbx1
Tdp1
Ube2v2
Polr2l
Nthl1
Ercc5
Uba52
Kat5
Slx1b
Polr2e
Log2FC: −2 +2
−Log10(FDR): >0 >1.3
Not detected:
C
SASP factors:
Liver
Lung
Kidney
Il6
Il1a
Il1b
Tnf
Ccl2
Ccl5
Ccl7
Cxcl1
Cxcl2
Cxcl5
Cxcl10
Mmp2
Mmp3
Mmp9
Mmp12
Mmp13
Mmp19
Timp2
Timp3
Igfbp2
Igfbp3
Igfbp5
Tgfb1
Tgfb2
Csf1
Csf2
Serpine1
Serpine2
Fn1
D
SA-β-Gal
TA
Ccne1T

Supplementary Figure 8. Cyclin E1 induces widespread transcriptional changes selectively in the liver. (*A*) Heatmap of up-regulated differentially expressed genes (DEGs) for the indicated annotation. Depicted are $\log_2$ fold expression changes in *Ccne1*^{T} versus *TA* tissues (box color) and the significance per gene (box size). (*B*) Heatmaps of up-regulated DEGs for the indicated annotations of the 'DNA damage/repair' cluster. (*C*) Expression of selected secreted factors that are often part of the senescence-associated secretory phenotype (SASP). (*D*) Representative images of SA-β-Gal-stained of 4-month-old liver cryosections. Scale bar, 40 μm. Heatmap legends in (*A*) and (*C*) are as in (*B*).